RESERVOIR-WELLBORE COUPLED SIMULATION OF LIQUID LOADED GAS WELL PERFORMANCE

A Thesis

by

MUHAMMAD FELDY RIZA

Submitted to the Office of Graduate and Professional Studies of
Texas A&M University
in partial fulfillment of the requirements for the degree of

MASTER OF SCIENCE

Chair of Committee,	A. Rashid Hasan
Committee Members,	Peter Valko
	Thomas A. Blasingame
Head of Department,	A. Daniel Hill

December 2013

Major Subject: Petroleum Engineering

Copyright 2013

ABSTRACT

Liquid loading of gas wells causes production difficulty and reduces ultimate recovery from these wells. In 1969, Turner proposed that existence of annular two-phase flow at the wellhead is necessary for the well to avoid liquid loading. In this work we applied Turner's approach to the entire wellbore. Analysis of available data from literature showed that transition from annular flow occurs much earlier at well bottom than at the wellhead. This entire wellbore approach proved to be more accurate in predicting onset of liquid loading. In addition, we developed a simple pseudo-steady-state reservoir flow model that was seamlessly connected to a wellbore two-phase flow model. The model is capable of predicting the time a gas well will produce without getting loaded with liquid and the length of time it can produce since loading inception if no intervention is carried out. We were able to develop a normalized time function applicable many reservoirs that would be indicative of loading-free productive life of a gas well.

DEDICATION

This work is dedicated to my parents and my fiancé, Fitria Tiur Komalasari, for their love, support, and patience enable me to finish this thesis.

ACKNOWLEDGEMENTS

I would like to thank my academic advisor, Dr. Rashid A. Hasan for his valuable guidance throughout the course of this research and also the financial support that he provided. I would also like to thank Mr. Shah Kabir for his valuable feedback and comments that have shaped the work in this research, and also the Hess Corporation for the financial support they gave for this study.

I would like to thank to Dr. Thomas A. Blasingame and Dr. Peter Valko for serving as my committee members and for their helpful comments and suggestions.

I also want to extend my gratitude to the Fulbright committee, which provided the funding for my Master's degree in Texas A&M University. I would also want to express my gratitude to Mrs. Eleanor Schuler, Mrs. Cook, Zach Alger, IIE and Sponsored Student Program office for the advices and help they gave during my study at Texas A&M University.

Finally, thanks to my parents for their encouragement and support, to Fitri for her patience and love, to Dr. Hasan's group students for the valuable discussions, lastly to my Indonesian friends in College Station for the sincere friendship and support.

TABLE OF CONTENTS

LIST OF TABLES

Page

LIST OF FIGURES

CHAPTER I

INTRODUCTION AND STUDY OBJECTIVES

According to the EIA report (2011) natural gas from conventional and unconventional resources supplied 25% of US energy consumption by 2010, and is projected to fulfill 26 % of US energy supply by 2035. In the year 2012 itself, the US consumed 25,5 Tscf of natural gas, while the total gas production is only 25,3 Tscf. The abundance of conventional gas, tight gas, shale gas, and coal-bed methane has shaped the supply and demand equation of natural gas in the US. Since gas is a cleaner source of fossil fuel and supported with the advance technology in energy efficiency, energy experts believed we are heading to golden age of gas production (EIA, 2011)

Natural gas exists in reservoirs in different thermodynamic states: as dry gas, wet gas, and as retrograde-condensate. Each state has different characteristics and classified based on its composition and its PVT diagram. During the production of gas well, liquid would co-produced with gas. The source of liquid could be from condensed gas, condensed water, water coning, aquifer water, water produced from another zone, or free water from formation (Lea and Nickens 2004). It requires high velocity of gas to transport coproduced liquid to the surface. If the velocity of gas is drop to the point that it cannot carry the coproduced liquid to the surface, the liquid will start dropping to the bottomhole, or often called as liquid loading.

1.1 Problem Description

Liquid loading is the inability of a producing gas well to remove its coproduced liquids from the wellbore. This condition commonly occurs in late phase of gas wells. Liquid loading is initiated by the reversal flow of liquid to the bottomhole. The liquid as a droplet or film which flow reversely would accumulate on the bottomhole. Thus, it will impose back pressure to the sand-face and ultimately would cause higher pressure loss in the wellbore. The problems caused by liquid loading would reduce the deliverability of the gas well, causing the wellhead pressure to drop significantly, and kill the well prematurely. Hence, the presence of liquid loading problem could reduce the ultimate recovery of the gas well.

The well under liquid loading problem is characterized by a sharp decline in production, unstable gas production rate, presence of recorded pressure spikes, tubing pressure decreases, sharp distinct change in pressure showing up in pressure surveys , annular heading, and sudden cease in liquid production (Lea and Nickens 2004).

Neves and Brimhall (1989) explained the process of liquid loading in four major steps as follow:

1), At early stages, a gas well has enough energy, due to high initial reservoir pressure, to carry the liquids all the way to the surface. At this stage the gas velocity is greater than the critical velocity required to continuously remove the liquids in the gas stream and the liquid droplet is suspended and transported to the surface. As the gas

velocity is high, gas carried liquid as small mist-like droplet, thus the flow pattern on this stage is called mist-annular wellbore flow pattern (Fig. 1.1(a)).

2) As production continues, reservoir pressure declines, resulting in the decline of gas flow rate which induces a decrease in gas velocity in the well until the gas velocity falls below the critical gas velocity value, marking the onset of liquid loading (Fig. 1.1(b)). Consequently, liquid droplets suspended in the gaseous phase will begin to move downward. The liquid begins to accumulate at the bottomhole.

3) The accumulated liquid at the bottomhole causes back pressure to the reservoir, causing gas inflow to decline as the bottomhole pressure decreases which induces the decrease of drawdown pressure from reservoir to the wellbore. The in-situ gas velocity actually may increase because of the reduction of the effective area for the gas phase to flow due to the liquid accumulation. This phenomenon results in a larger pressure drop across the accumulated liquid at the bottomhole. The pressure drop increases until the downstream pressure reaches the pressure necessary to blow down the liquids up to the surface (Fig. 1.1 (c)).

4) The well cycles back and forth between the second and third stage. However as time passes, the time differential between produced liquid slugs at the surface become greater as a consequence of the time required by the reservoir to reach a pressure high enough to blow the liquid slugs up the string. Eventually, the additional backpressure exerted at the sand-face on the accumulated of liquid will overcome the available reservoir pressure; the well is unable to produce and dies (Fig. 1.1 (d)).

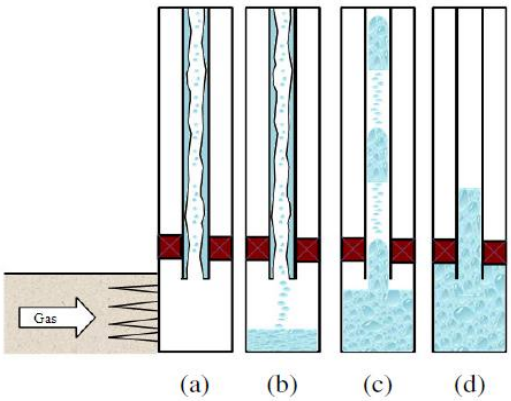

Fig 1.1 — Stages of liquid loading process. (a) 1st stage, (b) 2nd stage, (c) 3rd stage and (d) 4th stage (Fernandez et al. 2010)

1.1.1 Overview of Critical Loading Velocity Models

The understanding of the causes and symptoms of liquid loading and the behavior of gas well under liquid loading condition would provide a better insight to manage the gas well production, overcoming the liquid loading problem, and ultimately improve the recovery from the gas well.

Turner et al. (1969) proposed the first critical rate calculation to predict liquid loading. Turner's critical velocity model is based on a force balance of the largest possible droplet and the upward gas flow. The terminal velocity which suspends the biggest liquid droplet at the wellhead is called Turner's critical loading velocity.

Turner matched 66 of the tested 90 wells using its original critical velocity model, and 77 of 90 tested wells after an upward adjustment of 20%. Turner attributed the 20% adjustment to the use of drag coefficients for solid spheres rather than oscillating liquid drop, and the critical Weber number which was established for droplets in air experiment.

Numerous authors tried to revisit liquid loading prediction based on Turner's work (Table 1.1). Coleman et al. (1991a) suggested that Turner's 20% upward adjustment is unnecessary for gas wells with low gas rate and low wellhead pressure. Unfortunately, Coleman provided the database from very low wellhead pressure gas wells which suggested that the wells are already in dying condition.

Nosseir et al. (2000) matched Coleman's field dataset by adjusting the critical velocity model with flow regime. They proposed two critical velocity models; one for laminar flow regime, and one for highly turbulent flow regime.

Zhou and Yuan (2010) stated that liquid holdup is the third mechanism which cause liquid loading. They proposed two models separated by the threshold liquid holdup value. Below the threshold liquid holdup value, the critical velocity model is the same as Turner's model. Above the threshold liquid holdup value, the critical velocity model depends on the value of liquid holdup. All the critical liquid velocity models explained above were modified from Turner's droplet model.

However, Turner's classical work was limited by the technology at that time. The simplistic use of wellhead conditions to calculate liquid loading will give incorrect liquid loading rate prediction for some cases; for instance for wells installed with different tubing sizes, wells installed with tapered string, or if the tubing is set way higher than the perforation depth (Sutton et al. 2010).

The recent paper by van't Westende (2008) shed the lights about the actual mechanism which cause liquid loading. Van't Westende conducted multiphase flow

experiments and observed the phenomenon that occurs when reducing gas velocity in a flow-tube experiment. On the basis of measurements of droplet size and droplet velocity, van't Westende concluded that liquid loading corresponds with film flow reversal (Fig 1.2). Additionally, the film-flow reversal phenomenon coincides with the transition from annular flow to churn flow**.**

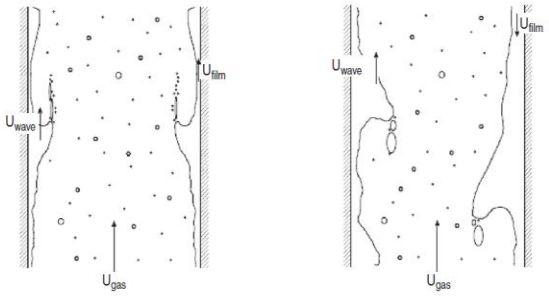

Fig. 1.2 — Transition from Annular to Churn flow triggers the liquid film flow reversal (van't Westende, 2008)

Veeken et al. (2010) reached similar conclusions by modeling the liquid-loading process using transient multiphase flow commercial software. Alamu (2012) conducted similar experiments and concluded that the liquid loading occurs at co-current annular and churn transition.

Sarica et al. (2013) conducted multiphase flow experiments for the vertical and deviated pipes and observed the same conclusion. They concluded that flow pattern transition from fully co-current annular flow to partially co-current annular flow triggers the initiation of film-flow reversal for vertical and deviated wellbores. Therefore, the

studies by the later authors strengthen the notion that liquid loading is tied to film-flow reversal.

Table 1.1 — Critical Velocity Models Comparison

Reference	Critical Velocity (V_c) [ft/s]	Note
(Turner et al. 1969)	$V_{TM} = 1.8949\left[\sigma\frac{(\rho_l - \rho_g)}{{\rho_g}^2}\right]^{0.25}$	Terminal velocity to suspend the biggest liquid droplet on wellbore
(Coleman et al. 1991a)	$V_{Co} = 1.5934\left[\sigma\frac{(\rho_l - \rho_g)}{{\rho_g}^2}\right]^{0.25}$	No need for 20% adjustment for wells with low wellhead pressure
(Nosseir et al. 2000)	$V_{No} = 1.356\left[\sigma\frac{(\rho_l - \rho_g)}{{\rho_g}^2}\right]^{0.25}$ $V_{No} = 1.978\sigma^{0.35}\frac{(\rho_l - \rho_g)^{0.21}}{\mu^{0.134}{\rho_g}^{0.134}}$	For transient flow regime ($N_{Re} > 1000$) For highly turbulent condition ($N_{Re} < 1000$)
(Zhou and Yuan 2010)	$V_{Zh} = 1.8949\left[\sigma\frac{(\rho_l - \rho_g)}{{\rho_g}^2}\right]^{0.25}$ $V_{Zh} = 1.8949\left[\sigma\frac{(\rho_l - \rho_g)}{{\rho_g}^2}\right]^{0.25} + ln\frac{y_l}{0.01} + 0.6$	For liquid holdup below the threshold ($y_l \leq 0.01$) For liquid holdup above the threshold ($y_l > 0.01$)

1.1.2 Overview of Liquid Loaded Gas Well Simulation Studies

Sharma et al (2013) studied the impact of liquid loading to productivity of hydraulically fractured shale gas well as well as the causes of liquid loading in shale gas wells. They concluded that several factors play important role in liquid loading occurrence in hydraulically fractured shale gas wells: low drawdown, high fracture permeability, low fracture height, and low matrix permeability. Additionally, matrix permeability reduction was found to be the worst factor which causes liquid loading as the decrease of permeability is directly correlated with gas velocity reduction. .

Dousi et al. (2006) proposed analytical reservoir-wellbore simulation to forecast gas production under liquid loading condition. They also introduced the term meta-stable gas rate, which is the gas rate at which the rate of liquid accumulated at the well bottom and liquid re-injected into the formation are equal, leading to accumulation of a stable water column at the wellbore.

Bin Hu et al. (2010) performed reservoir-wellbore coupled simulation to predict the liquid loaded gas well performance and its liquid cycling ability. The intermittent shut-in and production cycle operation on liquid loaded gas well is proven to be effective for eliminating the accumulation of a liquid column; thereby increasing the recovery of a liquid-loaded gas well.

Zhang et al. (2010) performed transient wellbore-reservoir coupled simulation to predict the bottomhole flowing pressure oscillation in the near-wellbore area, which was

caused by the reinjection and production cycles of liquid accumulated at the bottomhole into the reservoir.

Jackson et al. (2011) performed transient wellbore-reservoir coupled simulation of liquid loaded horizontal tight gas well. They studied the impact of liquid loading to horizontal gas well's productivity impairment, as well as sensitivity study of the impact of liquid loading to wellbore with different trajectories. The summary of liquid loaded gas well simulation studies by the past investigators are exhibited on Table 1.2 bellow.

However, none of these authors attempted to determine a well's liquid loaded-free life. In this work we looked at fluid flow from reservoir to surface as a seamless process to determine a well's liquid loaded-free life. In addition, we applied the concept that transition from annular flow at any point in the wellbore – not just at the wellhead – as the onset of liquid loading.

Indeed, because of lower gas velocity, the transition from annular two-phase flow is much more likely to occur at the bottomhole than at any other place in the wellbore. Once the flow pattern has changed from annular flow, it is only a matter of time for full-blown liquid loading to happen. We use Turner's original criterion, (without the 20% upward correction) as the condition for transition to/from annular two-phase flow.

Table 1.2 — Liquid Loaded Gas Well Simulation Study		
Reference	**Simulation Case**	**Significant Results**
(Dousi et al. 2006)	Numerical and analytical reservoir-wellbore coupled simulation modeling water accumulation and reinjection to the reservoir	Introduction of meta-stable gas rate for liquid loaded gas well
(Hu et al. 2010)	Numerical reservoir-wellbore coupled simulation of cycled intermittent production of liquid loaded gas well	Well production cycling could increase the production rate and improve the recovery of liquid loaded gas well
(Zhang et al. 2009)	Numerical reservoir-wellbore coupled simulation to predict the dynamic interaction between reservoir and wellbore during liquid loading	The pressure over distance profile of liquid loaded gas well shows U-shaped due to the impact of liquid accumulation to the near wellbore area
(Jackson et al. 2011)	Transient multiphase simulation of liquid loaded tight gas horizontal well's performance	Studied the impact of liquid accumulation to reservoir inflow performance distribution for horizontal tight gas well with different trajectories
(Sharma et al 2013)	Simulation of liquid loading effect to hydraulically fractured shale gas well's productivity	Matrix permeability reduction impact well's productivity severely, hence, might be the primary cause of liquid loading in shale gas well

1.2 Research Objectives

The purpose of this research is to provide a robust transient reservoir-wellbore coupled simulation to predict gas well performance under liquid loading problem. We also modeled rigorous heat transfer calculation and fluid properties correlations from the bottomhole to the wellhead to accurately modeling the wellbore flow pattern transitions on the wellbore.

This approach gives a comprehensive understanding of the behavior of liquid loaded gas well and allows us to forecast the life-time of the well if liquid loading starts occurring. Hence, further objectives of this research involve:

1. Investigate the causes of liquid loading, and also the parameters which affecting the critical loading velocity calculation
2. Provide a robust critical loading rate calculation and validate the model with critical liquid loading databases available on the literatures.
3. Perform comparison study of the proposed critical loading velocity model with other critical loading velocity models which proposed by previous investigators
4. Simulate gas well production performance under liquid loading condition and gives prediction of the time of the onset of liquid loading

CHAPTER II

MODEL DEVELOPMENT

Our goal is to understand and estimate the performance of a gas well under liquid loaded condition. To achieve this goal, we have used a simple analytic reservoir model coupled with a wellbore model. In this chapter, we discuss the mathematical formulation of the reservoir inflow performance and two phase flow in wellbore.

2.1 Reservoir Analytical Model

2.1.1 Reservoir Inflow

We develop an analytical gas reservoir inflow model connected to an analytical wellbore model to simulate the process of liquid loading and the performance of gas well production under liquid loading problem. Since liquid loading mostly happens in the late phase of conventional gas well, we assume that the well's drainage has already reached reservoir boundary. Hence, the pseudo-steady state inflow equation is used to model the gas inflow from the reservoir. Gas production inflow performance is calculated by the following expression

$$q_g = J_{PSS}\left(\bar{p}^2 - {p_{wf}}^2\right) \tag{2.1}$$

Where J_{PSS} is the Productivity Index of the gas well for pseudo-steady state condition, $\bar{p}$ is the average reservoir pressure, and p_{wf} is the bottom-hole flowing pressure.

We calculate liquid production rate by assuming liquid sources are condensed water and condensed gas only. We assume constant Water/Gas Ratio (WGR) and constant Condensate Gas Ratio (CGR) for the forecasting purpose. To simplify the inflow calculation, water aquifer and water coning effect is neglected in our reservoir model. Therefore, the water production rate is given by

$$q_{water} = q_g x WGR \tag{2.2}$$

Similarly liquid condensate production rate is given by

$$q_{cond} = q_g x CGR \tag{2.3}$$

2.1.2 Gas Material Balance Analytical Simulation

Gas reservoir fluid is assumed as wet gas reservoir; meaning gas presence as single phase gas in reservoir condition and liquid will yields as the reservoir pressure drops bellows bubble point pressure. We assume the reservoir behaves as a perfect single material balance tank. Therefore, we do not discretize the reservoir into several different grids to simplify the reservoir inflow performance.

We used material balance approach to forecast average reservoir pressure for time step n as given by the following expression

$$\frac{\bar{P}_n}{\bar{z}_n} = \frac{P_i}{Z_i}\left(1 - \frac{Gp_{T_n}}{G_i}\right) \tag{2.4}$$

Where the total cumulative gas production (Gp_T) is the sum of cumulative dry gas production (G_p) and gas-equivalent condensate liquid production

$$Gp_{T_n} = G_{p_n} + GE * N_{p_n} \tag{2.5}$$

GE is defined as gas-equivalent stock tank liquid production ratio and given by the following expression (Zeidouni et al. 2006)

$$GE = 133000 \frac{\gamma_c}{M_{wc}} \tag{2.6}$$

γ_c is the specific gravity of condensate liquid gathered from compositional analysis of surface condensate production. We can also estimate γ_c using the following expression

$$\gamma_c = \frac{141.5}{131.5 + API_{cond}} \tag{2.7}$$

Mw_c is the molecular weight of condensate liquid which determined from compositional analysis of condensate fluid. If there is no laboratory experiment performed, we can approximate Mw_c using the expression given bellow

$$Mw_c = \frac{42.43\gamma_c}{1.008 - \gamma_c} \tag{2.8}$$

We calculate initial gas in place (*Gi*) using volumetric method which given by the following expression

$$G_i = \frac{Ah\phi(1 - S_{wi})}{B_{gi}} \tag{2.9}$$

Hence, to calculate initial gas in place using volumetric method, we have to predict reservoir drainage area (*A*), reservoir thickness (h), formation porosity (ϕ), and initial water saturation (S_{wi}). Note that the initial formation volume factor (B_{gi}) in Eq. 2.9 is given by the following expression

$$B_{gi} = \frac{P_{sc}T_f}{T_{sc}P_i} Z_i \tag{2.10}$$

2.2 Wellbore Model

The reservoir model is connected to the wellbore model using a seamless computational approach. The well tubular consists of production tubing and casing. The schematic of the reservoir-wellbore connection is illustrated on Fig. 2.1 as follows

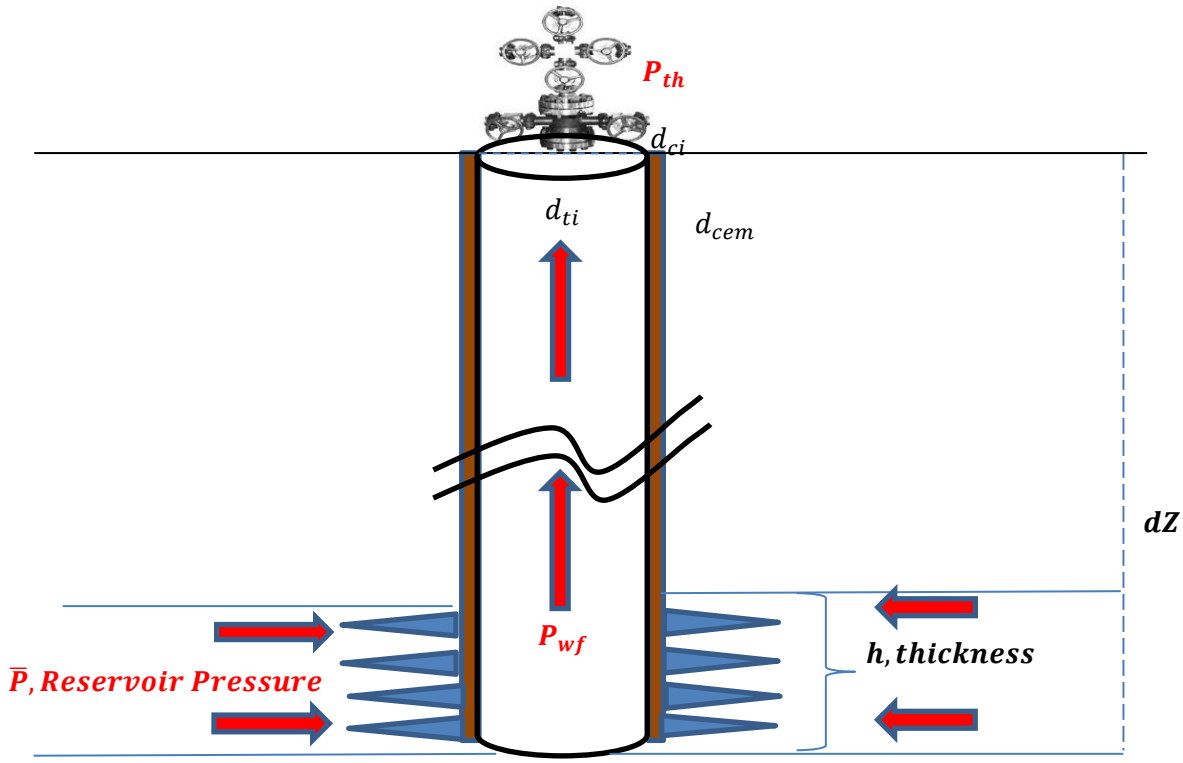

Fig. 2.1 — Illustrated reservoir – wellbore coupled model

The model is applicable for single phase gas flow, single phase liquid flow, and also multiphase flow. The wellbore model is discretized into 40 different sections to increase the accuracy of multiphase flow pressure loss calculation. The discretization also helps scrutinizing the flow regime transitions which occurs from the bottomhole to the wellhead.

During the co-current upward gas production, gas is flowing from the reservoir to the perforation sand-face then moving upward from the bottomhole of the wellbore to the surface. The inflow phenomenon from the reservoir to the wellbore is expressed as the deliverability equation which expressed in Eq. 2.1. The reservoir drawdown pressure implies the difference between reservoir pressure $(\bar{p})$ and the bottomhole flowing

pressure (p_{wf}), while the outflow performance defined as the pressure losses occurs from the bottomhole (p_{wf}) to the wellhead (p_{th}) during the production.

2.2.1 Pressure Loss Calculation

The general momentum balance equation for multi-phase compressible fluid, for the section where no shaft work is added, is expressed by

$$\Delta P = \frac{g}{g_c}\bar{\rho}_m dz + \bar{\rho}_m \frac{\Delta {v_m}^2}{2g_c} + \frac{2f_m \bar{\rho}_m {v_m}^2 dz}{g_c d} \tag{2.11}$$

or,

$$\Delta P = \Delta P_H + \Delta P_{KE} + \Delta P_f \tag{2.12}$$

The static, kinetic, and friction heads are,

$$\Delta P_H = \frac{g}{g_c}\bar{\rho}_m dz \tag{2.13}$$

$$\Delta P_f = \frac{2f_m \bar{\rho}_m {v_m}^2 dz}{g_c d} \tag{2.14}$$

$$\Delta P_{KE} = \bar{\rho}_m \frac{\Delta {v_m}^2}{2g_c} \tag{2.15}$$

In these expressions v_m and ρ_m are mixture velocity and density, g is the gravitational constant and f_m is the applicable friction factor

During multiphase flow, the wellbore is simultaneously occupied by flowing liquid and gas. Thus, neither phase occupies the entire wellbore cross section. The

fraction of the pipe cross-section occupied by the gas is termed gas void fraction (f_g) while, liquid holdup (f_l) is defined as the wellbore cross-section occupied by liquid. Hence,

$$f_l = 1 - f_g \tag{2.16}$$

Gas void fraction depends on several parameters; two phase flow pattern, inclination of wellbore, and direction of flow. Two phase flow pattern and its gas void fraction would be discussed with more details in a later section.

Fluid mixture density ($\bar{\rho}_m$) is calculated by adding the gas density (ρ_g) and liquid density (ρ_l) times the volume fraction that each phase occupies. Thus,

$$\bar{\rho}_m = f_g \rho_g + \rho_l f_l \tag{2.17}$$

The in-situ mixture velocity (v_m) is the total of of gas (v_{sG}) and liquid (v_{sL}) superficial velocities,

$$v_m = v_{SL} + v_{SG} \tag{2.18}$$

We calculate two phase flow friction factor (f_m) in conduit using Chen (1979) correlation given by

$$f_m = \frac{1}{4log\left(\frac{\frac{\varepsilon}{d}}{3.7065} - \frac{5.0452}{Re_m} log\Lambda\right)^2} \tag{2.19}$$

In Eq. 2.19 ε is the pipe roughness, d is the pipe diameter, Re_m is Reynold number for two phase flow, and Λ is a dimensionless parameter. The dimensionless parameters Λ and Reynold's number (Re_m) are given by

$$Re_m = \frac{\rho_m v_m d}{\mu_m} \tag{2.20}$$

$$\Lambda = \frac{(\varepsilon/d)^{1.1098}}{2.8257} + \left(\frac{7.149}{Re_m}\right)^{0.8981} \tag{2.21}$$

2.2.2 Two Phase Flow Patterns

The variety of liquid rates, gas rates, fluid properties, pipe inclination, and flow direction allows different flow patterns to exist on a wellbore. Fig 2.2 illustrates the major multi-phase flow patterns in vertical upward flow – bubbly, slug, churn, and annular. Bubbly or dispersed-bubbly flow pattern is rarely occurs in gas wells.

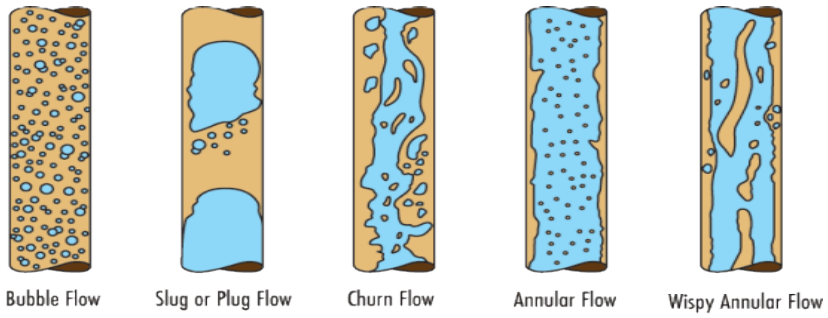

Fig. 2.2 — General two phase flow patterns in vertical upward wellbore two phase flow (Kang, 2008)

During gas-liquid flow, gas generally moves faster than liquid because it is lighter and has a tendency to flow at the center of the pipe. Liquid phase generally flows as droplets, slug, or liquid films. As Hasan and Kabir (2002) explains the in-situ gas velocity can be expressed as the sum of the bubble rise velocity (v_∞) and the channel center mixture velocity ($C_o v_m$). Therefore, gas void fraction can be expressed by the following expression

$$f_g = \frac{v_{SG}}{C_o v_m + v_\propto} \tag{2.22}$$

The flow parameter (C_o) depends on flow regime, well deviation, and flow direction. For turbulent flow, the mixture velocity profile is relatively flat and the velocity at the center of the wellbore is 1.2 times the average mixture velocity. In bubbly and slug flow, most of the gas bubbles flow through the center of the pipe, thus C_o = 1.2 for these two flow regimes. Churn flow is characterized by high turbulence which breaks up the Taylor bubble and cause both gas and liquid phases to be dispersed. Thus, a slightly lower value of 1.15 is used for C_o for churn flow. For annular flow Hasan et al. (2007) suggested that there is no slippage, and that C_o equals 1.0.

The flow parameters (C_o) values and bubble rise velocites (v_∞) for each flow pattern are summarized in Table A.1. The expressions for bubble rise velocities are detailed in APPENDIX A.2.

Two phase flow regime and its transition criteria have been studied extensively by numerous authors. We used Hasan-Kabir's approach to determine flow pattern

transitions that are detailed in APPENDIX A.3. Briefly, we used transition from bubbly to slug flow to occur if gas void fraction exceeds 0.25 in vertical pipes. Transition from slug flow to churn flow occurs if v_m exceeds a certain value (about 10 ft/s) detailed in APPENDIX A.3. The transition from churn to annular flow occurs if v_{sg} is higher than the critical velocity given by the following expression

$$v_{gc} = 3.1\left[\frac{g(\rho_l - \rho_g)\sigma}{{\rho_g}^2}\right]^{0.25} \tag{2.23}$$

Since annular flow is characterized by the liquid film flowing on the wall of the pipe, a minimum gas void fraction ($f_{g_{Min}}$) of 0.6 is required to sustain the liquid film from bridging the cross-section of the channel. The smoothing of flow patterns transitions are summarized on APPENDIX A.4.

2.3 Heat Transfer Model

A robust heat transfer model is critical to accurately calculate reservoir fluid properties, and critical loading velocity. We used an analytical heat transfer model for complex wellbore which proposed by Hasan et al. (2009) for this study. APPENDIX A.5 explains the detail of analytical heat transfer model for two phase liquid and gas flow.

The wellbore model consists of heat transfer from reservoir to the wellbore radially and also vertically**.** In vertical well, the differential of flowing fluid temperature equation (T_f) over the distance *z* is given by the following expression

$$\frac{dT_f}{dz} = L_R\left(T_f - T_{ei}\right) + \frac{g\ sin\ (\theta)}{C_p J g_c} - \phi \tag{2.24}$$

Where the variable ϕ lumps the kinetic energy term and the term containing the Joule-Thompson effect

$$\phi = \frac{v}{C_p J g_c}\frac{dv}{dz} - C_j \frac{dp}{dz} \tag{2.25}$$

The relaxation parameter, L_R (Hasan et al., 2007), which is the inverse of the parameter A, which given by Ramey (1962) is given by the following expression

$$L_R = \frac{2\pi}{wc_p}\left(\frac{r_{to}U_{to}k_e}{k_e + r_{to}U_{to}T_D}\right) \tag{2.26}$$

Where T_D is given by

$$T_D = ln\left[e^{(-0.2t_D)} + (1.5 - 0.3719e^{-t_D})\right]\sqrt{t_D} \tag{2.27}$$

The constant T_{ei} in Eq. 2.48 represents the undisturbed earth temperature which for well with inclination θ, the earth temperature is expressed by

$$T_{ei} = T_{ei_{wh}} + zg_G sin\ (\theta) \tag{2.28}$$

Assuming other terms other than T_f in Eq. 2.48 is invariant with depth (z), we can rearrange Eq. 2.37 into first order differential equation

$$T_f = T_{ei} + \frac{1 - e^{(z-z_j)L_R}}{L_R}\left(g_G sin\,(\theta) + \phi - \frac{g\,sin(\theta)}{C_p}\right) + e^{(z-z_j)L_R}\left(T_{f_j} - T_{ei_j}\right) \tag{2.29}$$

2.4 Critical Loading Velocity Model Development

In the late sixties, Turner (1969) pioneered the use of critical loading velocity to determine whether a well is liquid loaded using liquid droplet flow reversal model and adjusted it 20% upward

$$V_{TM} = 1.8949\left[\sigma\frac{(\rho_l - \rho_g)}{{\rho_g}^2}\right]^{0.25} \tag{2.30}$$

However, because of computational difficulties, Turner used Eq. 2.35 to the wellhead conditions and were able to match 66 out of 106 field data. Sutton et al. (2010) observed that the use of wellhead data to calculate critical loading rate could sometimes be misleading and suggested that the use of bottomhole conditions would give more accurate predictions.

We believe that the entire wellbore must be in annular flow pattern for a well to be free from liquid loading. The occurrence of slug or churn flow anywhere in the wellbore would indicate that the well is undergoing liquid loading. Because the pressure is highest, and hence gas velocity is perhaps lowest at the bottomhole, transition from annular flow is most likely to occur at the bottomhole first, as Sutton surmised.

Therefore, we approach the liquid loading problem by investigating the two phase flow pattern throughout the entire wellbore. We use Turner's original equation to calculate liquid loading as it coincides with annular-churn critical velocity. We expect

churn or slug flow pattern to be established at the bottomhole first while rest of the wellbore still exhibits annular flow. Once this has happened, liquid loading has been initiated, and it's a matter of time that the well will kill itself unless there is some sort of intervention.

To accurately model the full-wellbore critical velocity, we need an accurate knowledge of fluid properties and wellbore temperature since surface tension (σ), gas density (ρ_g), and liquid density (ρ_l) vary with pressure, and temperature on the wellbore. The fluid properties correlations used to develop full-wellbore critical velocity analysis is detailed in APPENDIX B.

CHAPTER III

MODEL IMPLEMENTATION AND DATA VALIDATION

In this chapter we implement the wellbore fluid and heat flow model using the actual field data set. We identify two phase flow patterns in the entire wellbore of the liquid loaded gas wells. Consequently we validate the theory that the entire wellbore should be in co-current annular to avoid liquid loading with databases available on the literature.

3.1 Data and Assumptions

In this section, we implement the wellbore/reservoir model using the data of an actual liquid loaded gas well from Veeken's thesis (2010). Since the Author did not publish liquid gas ratio, liquid gas density, and complete wellbore configuration data, we have to make some assumptions in order to perform the full-wellbore pressure loss and critical liquid loading analysis. The well data set are summarized in Table 3.1, and the heat and wellbore properties are summarized in Table 3.2.

We use the average deviation as the total deviation of the wellbore. We assume that completion diameter is the tubing diameter and we only use completion diameter throughout the calculation as there is no information of the complete section of wellbore diagram. We converted the data set from Veeken's thesis from Metric unit to US Field Units.

We assume the reservoir only produces water and not condensate liquid. Water-gas ratio is assumed 80 STB/MMSCF. These and other assumptions we used for calculation are summarized in Table 3.3.

Table 3.1 — Well #19 Dataset (Veeken et al. 2010)

Parameters	Value	Units
Well True Vertical Depth (TVD)	6561.68	ft
Tubing Inside Diameter	4.89	in
Reservoir Diameter	6.88	in
Bottomhole Temperature	125.6	°F
Well Deviation	19	°
Gas Specific Gravity, Υ_g	0.59	-
Wellhead Pressure	87	Psi
Formation Resistivity , A	20.25	Psi^2/MSCF/D
Productivity Index, J (1/A)	0.049	MSCF/D/Psi^2
Wellhead Temperature	60.8	°F
Q Min	2224	MSCF/D
Q Turner	2099	MSCF/D

Table 3.2 — Heat and Wellbore Properties

Parameters	Value	Units
cpo	0.53	Btu/lb/F
cpw	1.00	Btu/lb/F
cpg	0.51	Btu/lb/F
cpann	0.61	Btu/lb/F
k_t	26	Btu/hr-ft-F
k_f	0.2	Btu/hr-ft-F
kcas	26	Btu/hr-ft-F
k_{ann}	0.3	Btu/hr-ft-F
k_{form}	1.4	Btu/hr-ft-F
k_{cem}	1	Btu/hr-ft-F
dci	8	in
dco	9	in
dcemo	24	in
Pipe Roughness (ε)	6.00E-05	-

Table 3.3 — General Assumptions	
Parametes	**Value**
Υ_w	1.06
CGR	0 STB/MMSCF
WGR	80 STB/MMSCF

3.2 Model Implementation

The wellbore pressure profile is graphed in Fig. 3.1. Given the tubing head pressure of the well is 87 psi and the observed liquid loaded gas rate (Q Min) is 2224 MSCFD, the bottomhole flowing pressure calculated using Hasan-Kabir model is 727 Psi. The wellbore pressure profile shows two distinct pressure gradient trends, thus, indicating flow patterns transition that occurs during liquid loading. Fig. 3.2 exhibits the calculated top-down wellbore temperature profile using the Hasan-Kabir model.

Fig. 3.3 depicts water-gas surface tension profile with wellbore flowing temperature (T_f) and total vertical depth (TVD). We can see that the surface tension is decreasing as temperature and pressure decrease.

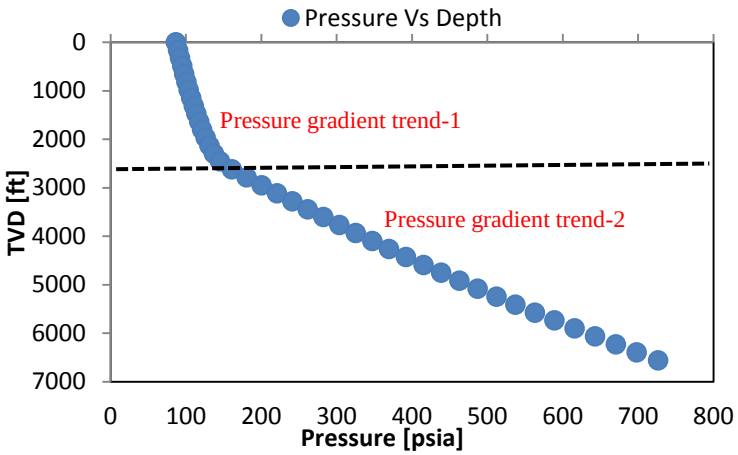

Fig. 3.1 — True Vertical Depth (TVD) vs. Wellbore pressure profile shows two distinct pressure gradients caused by the transitions of two different flow patterns on the wellbore

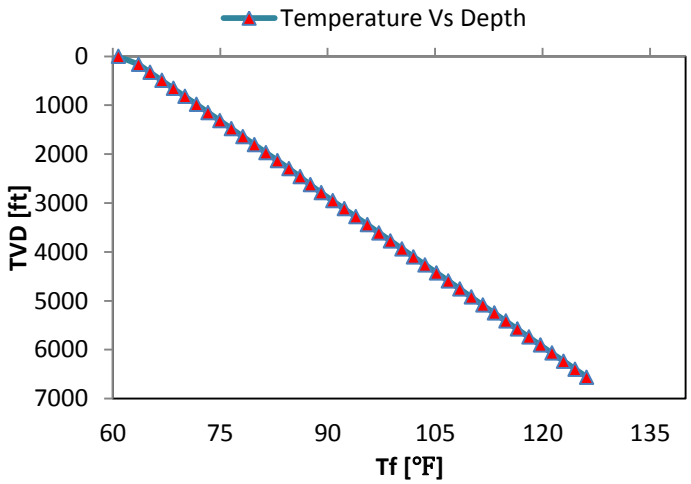

Fig. 3.2— Wellbore flowing temperature (T_f) profile on the wellbore using Hasan & Kabir model

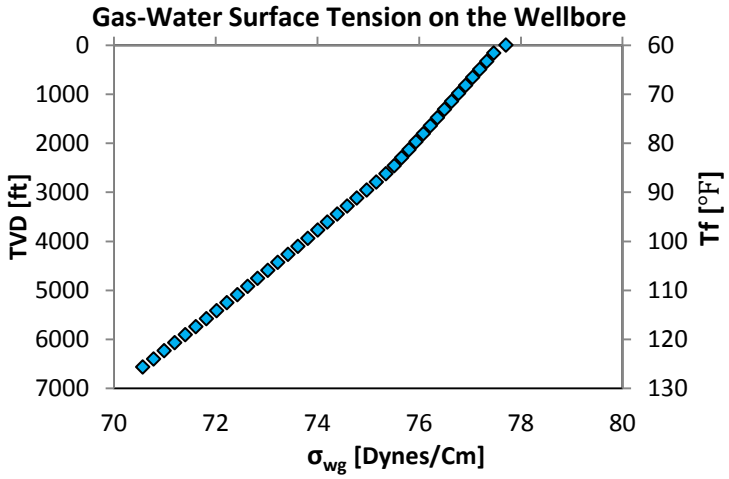

Fig. 3.3 — Gas-water surface tension (σ_{wg}) varies with depth and temperature profile on the wellbore. Gas-water surface tension (σ_{wg}) decreases as temperature Increases

3.2.1 Flow Pattern Identification

To understand the physical phenomenon which occurs during liquid loading, we analyze the flow pattern, liquid holdup, as well as the pressure gradient profile of the tested well. Fig 3.4 shows the superficial gas velocity and the critical transition velocity profile in the well. Gas superficial velocity (v_{SG}) is increasing from the bottomhole to the wellhead as wellbore flowing pressure is decreasing, thus, allowing gas to expand and accelerates. Using the Hasan-Kabir pattern transition criteria, we identified that the lower part of the wellbore is experiencing slug flow ($v_{SG} < v_{gc}$), while the upper part of the wellbore has annular flow ($v_{SG} > v_{gc}$).

Fig. 3.5 illustrates the pressure gradient components. The total pressure gradient consists of hydrostatic, frictional, and acceleration pressure gradient. However, we do not include the acceleration pressure gradient on Fig. 3.5 as it is very small. Hydrostatic

pressure gradient is observed to be the biggest contributor of the total pressure gradient, especially on wellbore section where slug flow occurs.

As suggested by the profile of liquid holdup (Fig 3.6), slug flow carries significantly higher liquid compared to annular flow. Higher liquid holdup will causes higher density of mixture, thus, higher hydrostatic pressure gradient.

Frictional pressure gradient increases from the bottomhole to the wellhead as the velocity of gas increases. Frictional pressure gradient then abruptly drops after the flow pattern evolves from slug to annular flow. This happens since gas void fraction (f_g) is increases as the flow regime changes from slug to annular flow, causing the mixture density to decreases significantly, consequently reducing the two phase friction pressure gradient.

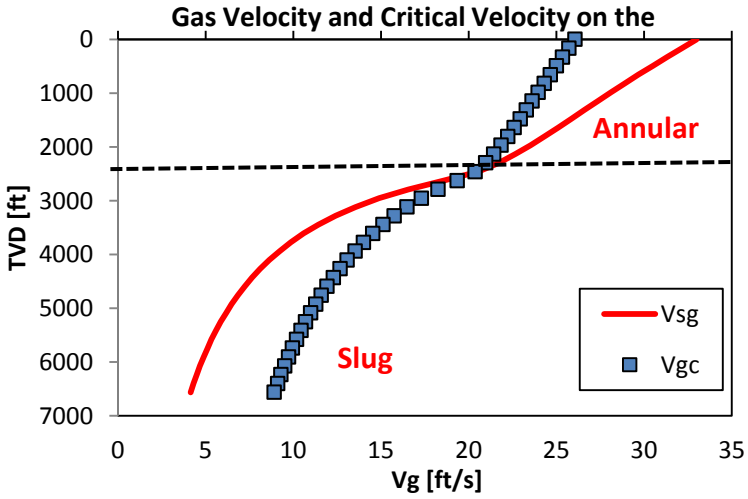

Fig. 3.4 — Gas velocity (v_{SG}) and critical Annular-Churn transition velocity (v_{gc}) profile on the wellbore indicates the impact of two phase flow patterns distribution on the wellbore to velocity profile

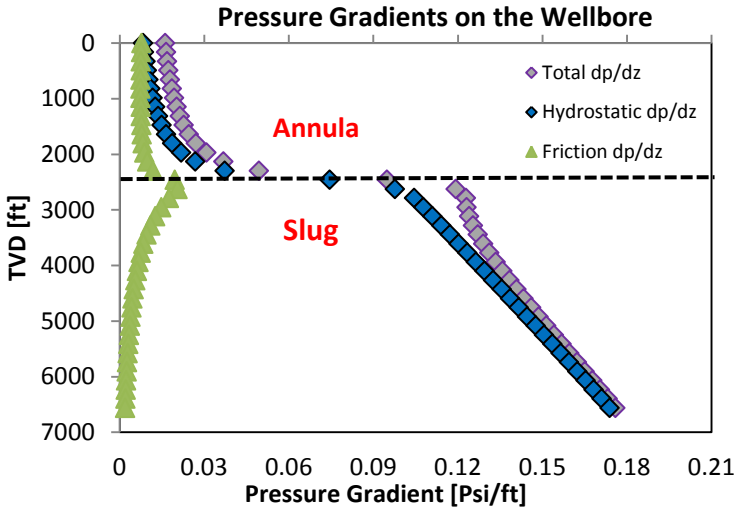

Fig. 3.5 — Pressure gradients profile on the wellbore show hydrostatic pressure gradient as the biggest component of total pressure gradient component

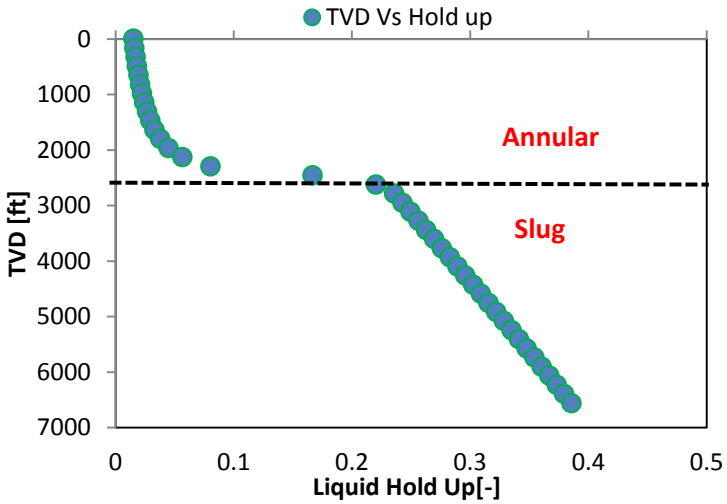

Fig. 3.6 — Liquid holdup (f_l) profile on the wellbore exhibits sudden increase of liquid holdup as flow pattern evolves from Annular to Slug Flow

3.2.2 Flow Pattern Transition and WGR Variation

Since there is no information of the actual Water/Gas Ratio (*WGR*) on Veeken's thesis, we investigate the impact of Water/Gas Ratio (*WGR*) variation on two-phase flow regime transition and liquid loading. Gas superficial velocity (v_{SG}) increases as gas flows from the bottomhole to the wellhead.

The impact of WGR variation to Liquid holdup profile is shown in Fig. 3.7. Liquid loading initiation is marked by sudden increase of liquid holdup which is caused by the transition from annular flow to slug flow. The effect of *WGR* variation seems insignificant to flow pattern transition, except if *WGR* is nearly 0 which cause the flow pattern to be fully annular.

The effect of WGR variation on hydrostatic pressure gradient is illustrated in Fig. 3.8. By increasing WGR immensely, we can see slight effect of increased liquid holdup and hydrostatic head. The friction pressure gradient vs. v_{SG} profile is depicted in Fig 3.9. The impact of WGR variation is seen more detrimental to friction pressure losses compared to hydrostatic pressure loss. Fig. 3.10 depicts the impact of WGR variation to total pressure gradient.

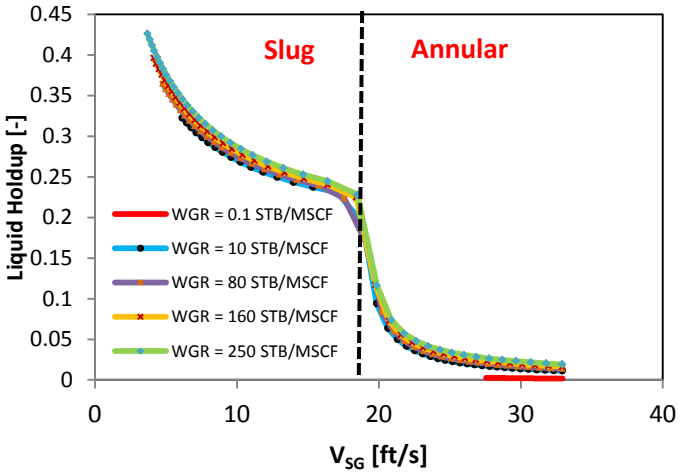

Fig. 3.7 — Sensitivity of Water/Gas Ratio (WGR) to liquid holdup Indicates WGR variation does not influence liquid holdup and the transition of flow pattern

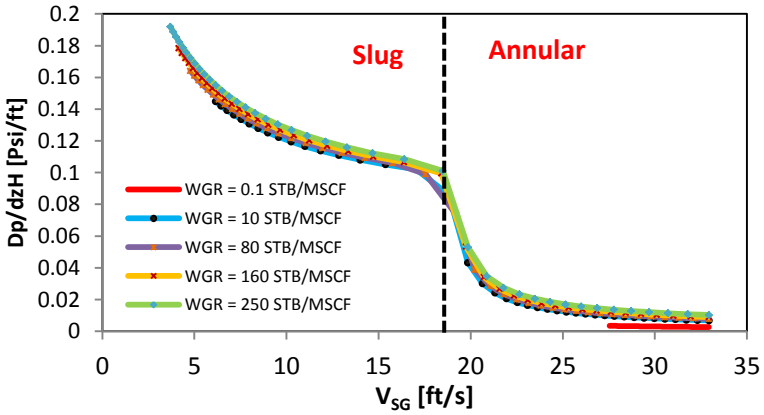

Fig. 3.8 — Sensitivity of Water/Gas Ratio (WGR) to wellbore hydrostatic pressure gradient shows little impact of WGR variation to hydrostatic pressure loss

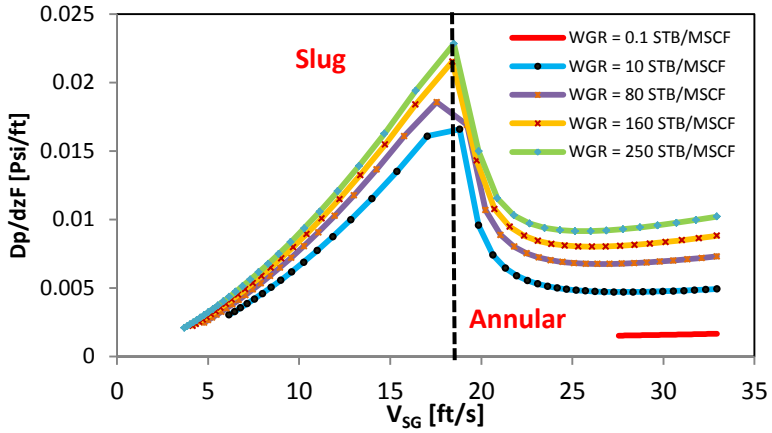

Fig. 3.9 — Sensitivity of Water/Gas Ratio (WGR) to frictional pressure gradient shows friction pressure loss is more sensitive to WGR variation compare to hydrostatic pressure loss

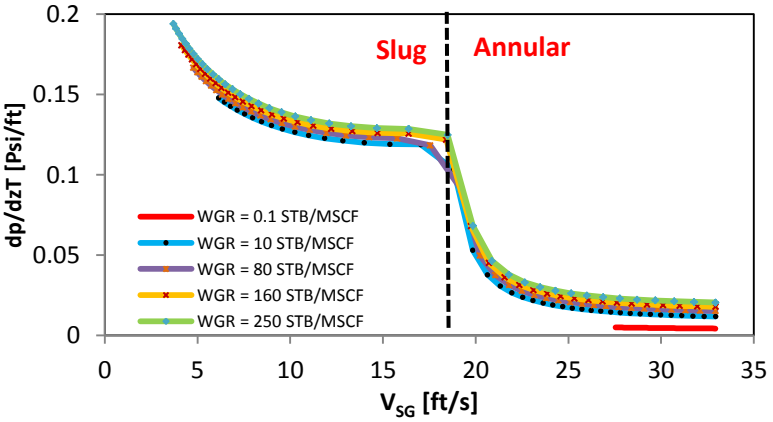

Fig. 3.10 — Sensitivity of Water/Gas Ratio (WGR) to total pressure gradient components (frictional, hydrostatic, and acceleration)

3.3 Critical Velocity Models Comparison

We plot gas superficial velocity (v_{SG}) with the various critical velocity calculated using various models for the entire wellbore on Fig. 3.11. We calculate surface tension using the correlation detailed in APPENDIX B.

The results suggest that there is no large deviation between Nosseir's critical velocity (v_{No}) and Turner's adjusted critical velocity model (v_{Tm}) for this well. This is caused by the combination of low gas rate and big wellbore diameter of the tested well resulting in low flow regime.

In the slug flow section of the wellbore, Zhou's critical velocity (v_{Zh}) deviates further from Turner's modified model (v_{Tm}). This happens because the liquid hold up (f_l) in slug flow section of the wellbore is higher than liquid hold up in annular flow and Zhou's model predictions depend on f_l. However, in the annular section of the wellbore, Zhou's model predicts numbers very close to that of Turner's model. Zhou's model gives the highest critical velocity calculation for this example case, while Coleman's model gives the smallest critical velocity prediction.

The results show that actual gas velocity (v_{SG}) at the wellhead is higher than liquid loading critical velocity predicted by all models. Therefore, although the well is actually loading up, none of the critical velocity models predict that the well is liquid loaded as they are based on the wellhead condition.

However, gas superficial velocity (v_{SG}) at the bottomhole is lower than the critical velocity predicted by all of the models. Therefore, we believe that bottomhole condition controls the initiation of liquid loading regardless of the tubing diameter variation on the wellbore as previously suggested by Sutton (2010). We summarize gas superficial velocity and critical loading velocity calculated using various models at the wellhead and bottomhole conditions in Table 3.4.

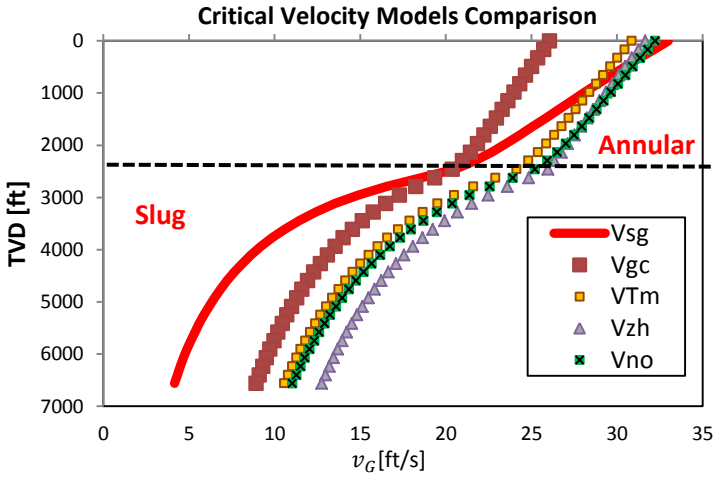

Fig. 3.11 — Gas superficial velocity (v_{SG}) and critical loading velocity models on the entire wellbore indicates misleading use of wellhead condition to predict liquid loading

Table 3.4 — Critical Velocity Models and Flow Pattern Well Veeken-#19

Reference	Flow Pattern	Actual Gas Velocity (ft/s)	Critical Velocity Models			
			Annular-Churn (ft/s)	Turner (ft/s)	Nosseir (ft/s)	Zhou (ft/s)
Wellhead	Annular	33	26.1	30.9	32.2	31.7
Bottomhole	Slug	4.2	8.9	10.6	11	12.8

3.3.1 Liquid Loading Initiation

We applied the similar approach to selected wells from Veeken's (2010), Coleman's (1991a), and Turner's (1969) liquid loaded gas wells databases. Note that, all the wells in Veeken's and Coleman's data are actually liquid loaded while 64% of wells in Turner's database are liquid loaded. Fig. 3.12 through Fig. 3.14 display the pressure profile and the critical velocity along with the superficial of gas velocity of the selected wells from different databases. The pressure loss calculation and gas velocity profile graphs are constructed using the actual observed liquid loading rate (q_{Test}) reported in the literatures.

Well #5 from Veeken's database (Fig. 3.12) and well #11 from Coleman's database (Fig. 3.13) show slug flow and churn flow pattern development on the wellbore which starting from bottomhole, while the wellhead is still in annular flow. Meanwhile, well #8 from Turner's database (Fig. 3.14) shows that the entire well is experiencing slug flow.

The results show that Turner's assumption to use wellhead condition to predict initiation of liquid loading leads to inaccurate predictions. Wellhead gas superficial velocities in all these wells except one (Turner-8) that show liquid loading symptoms are found to be higher than the critical loading velocity estimated by all models. Turner-8 is identified to have slug flow pattern throughout the entire wellbore. These results strengthen the notion that bottomhole of the wellbore controls initiation of liquid loading that we state on the previous section. The dataset used and the flow pattern analysis results are summarized in Table 3.5.

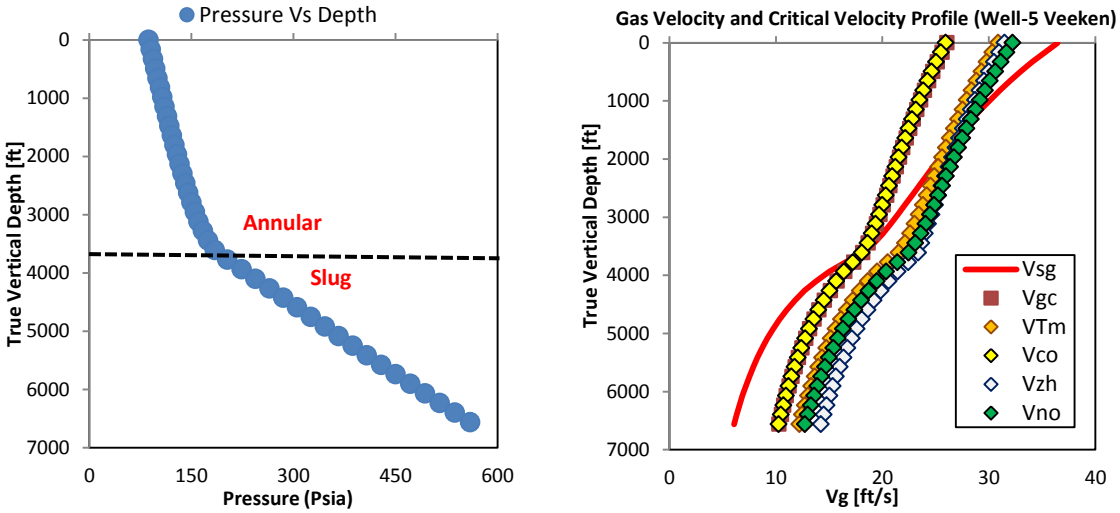

Fig. 3.12 — (Left) — Pressure gradient and flow pattern of Well Veeken-5. (Right) — Critical velocity and gas superficial velocity profile of Well Veeken-5

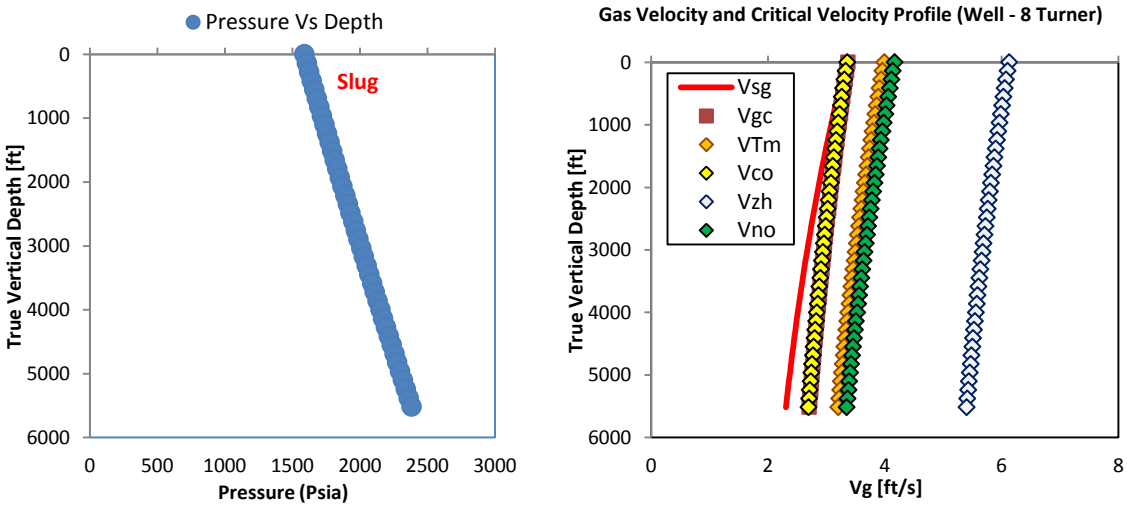

Fig. 3.13 — (Left) — Pressure gradient and flow pattern profile of Well Turner- 8. (Right) — Critical velocity and gas superficial velocity profile of Well Turner-8

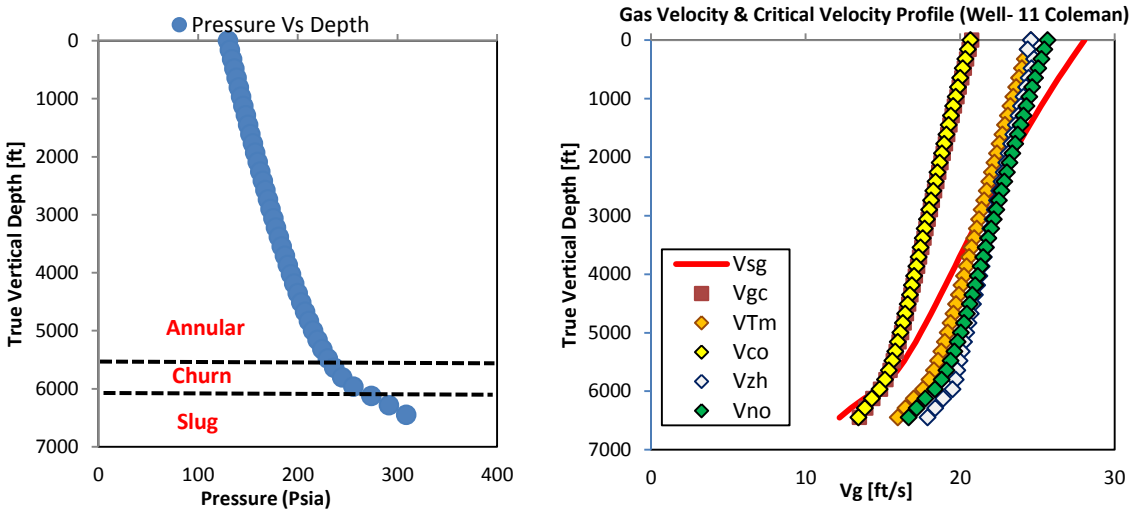

Fig. 3.14 — (Left) — Pressure gradient and flow pattern profile of Well Coleman-11. (Right) — Critical velocity and gas superficial velocity profile of Well Coleman-11

Table 3.5 — Liquid Loading Initiation Analysis

Well No.	qGas (MscfD)	TVD (ft)	Pth (psi)	Tub. ID (in)	Ref.	Flow Patt.	Vsg (ft/s)	Critical Velocity	
								Ann-Churn (ft/s)	Turner (ft/s)
Veek -#19	2225	6562	87	4.89	WH	Ann.	33	26.1	30.9
					BH	Slug	4.2	8.9	10.6
Veek -#5	919	6562	87	2.99	WH	Ann.	36.5	26.1	30.8
					BH	Slug	6.1	10.3	5.1
Turn -#8	3009	5515	1590	3.98	WH	Slug	3.3	3.4	4
					BH	Slug	2.3	2.7	3.2
Col-#11	635	6449	130	2.44	WH	Ann.	28.1	20.8	24.6
					BH	Slug	12.2	13.5	16

3.4. Model Validation

Turner (1969), Coleman (1991a), and Veeken (2010) published extensive databases for the purpose of liquid loading investigation. We verified the critical loading rate calculation using the proposed method (Section 3.2) and compare the results with the methods published by the previous investigators.

Liquid loading rate (qC) is observed and approximated using the bottomhole condition. We define the critical liquid loading rate as the rate at which slug or churn flow begins developing at the bottomhole of the wellbore, or

$$qC = 3.06 \frac{P_{wf} v_{gc_{wf}} A_{wb}}{(T_{wf_{\circ R}}) Z_{wf}} \tag{3.1}$$

Since all the databases used the wellhead condition to calculate critical liquid loading rate, we performed the top-down pressure loss, heat loss, and flow pattern identification to determine liquid loading using the proposed method.

3.4.1 Model Validation Using Turner's Database

Turner et al. (1969) were the first investigator of liquid loading prediction and published extensive database of liquid loaded gas wells. They published important parameters which influences critical liquid loading rate calculation; wellbore diameter, wellhead pressure, liquid gas ratio, and fluid properties.

Turner's critical loading rate prediction (q_{Turner}) is calculated by applying Eq. 3.2 at the wellhead condition,

$$qTurner = 3.06\frac{P_{wh}v_{TM_{wh}}A_{wb}}{(T_{wh_{\circ R}})Z_{wh}} \tag{3.2}$$

Fig. 3.15 depicts the relationship between the critical loading rates (qC) calculated using Eq. 3.1 vs. the actual liquid loading rate (q_{Test}) of 64 wells gathered from Turner's database. We do not validate the method on wells with questionable status and wells which produced through the annulus.

Based on the proposed method, all liquid loaded gas wells in Turner's database are predicted having slug flow and churn flow pattern in the well. Conversely, the unloaded gas wells are predicted as having annular flow throughout the entire wellbore. There are four liquid loaded wells that show annular flow on the entire wellbore, nevertheless, other wells are in good agreement with the condition that reported by Turner.

The relationship between Turner's adjusted droplet model (with 20% greater constant) calculated on the wellhead with the actual liquid loading gas rate (q_{Test}) is graphed in Fig**.** 3.16. We clearly see that Turner's 20% upward adjusted model gave a poor prediction to predict loading condition. Although all these wells were actually loaded up, Fig. 3.16 shows that Turner's adjusted model suggests quite a few of them are unloaded. The results of Turner's database validation are summarized on Table C-1 in APPENDIX C.

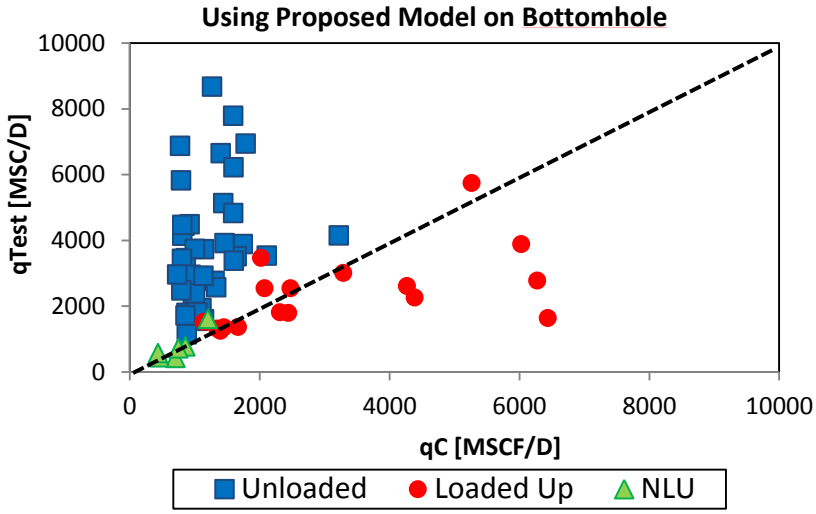

Fig. 3.15 — Relationship of actual liquid loading rate ($qTest$) vs. proposed critical liquid loading rate evaluated on the bottomhole (qC) suggests better correlation to predict liquid loading using bottomhole condition

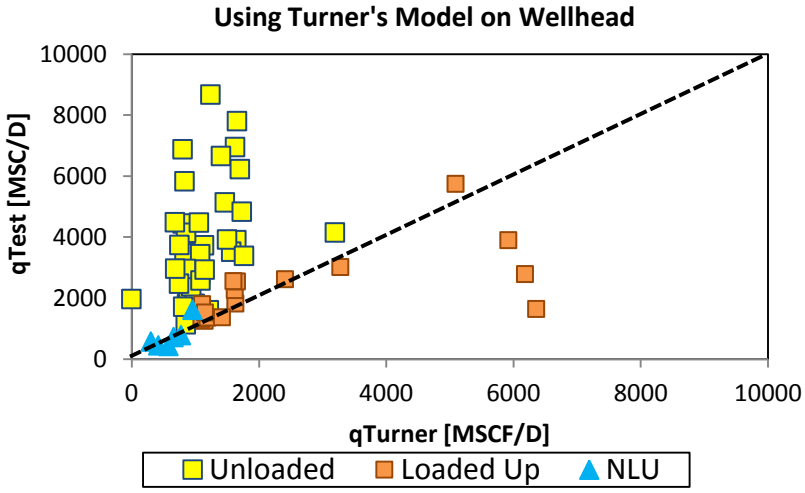

Fig. 3.16 — Relationship of actual liquid loading rate ($qTest$) with Turner's critical liquid loading rate calculated on the wellhead ($qTurner$) suggests Turner's modified critical liquid loading rate calculated on the wellhead miss-predicted some wells data points

3.4.2 Model Validation Using Coleman's Database

We validate the proposed critical liquid loading gas rate calculation with the database published by Coleman (1991a). Using the given information in the database, we matched the calculated bottomhole pressure with the measured static bottomhole pressure by adjusting the liquid density that were unavailable and liquid/gas ratio that were more unreliable than bottomhole pressure.

Coleman used the original Turner droplet velocity expression, Eq. 3.3, to calculate the critical loading velocity for low wellhead pressure and low gas rate wells

$$v_{Co} = 1.5934\left[\sigma\frac{(\rho_l - \rho_g)}{{\rho_g}^2}\right]^{0.25} \tag{3.3}$$

Fig. 3.17 depicts the relationship between the critical liquid loading rates calculated using Eq. 3.1 vs. the actual liquid loading gas rate ($qTest$). We identified 51 out of 55 liquid loaded gas wells having slug or churn flow starting to develop at the bottomhole. The four data points our approach missed are actually quite close with the critical annular-churn transition line. Thus, the proposed method correlates very well using Coleman's database.

The critical loading rates calculated by Coleman using the wellhead condition are plotted with actual liquid loading rate in Fig. 3.18. Here we can see that the use of wellhead condition to predict liquid loading result in poorer correlation compare to bottomhole. Table C-2 in APPENDIX C summarizes the calculated bottomhole pressure, critical loading rates, and predicted flow pattern on the bottomhole.

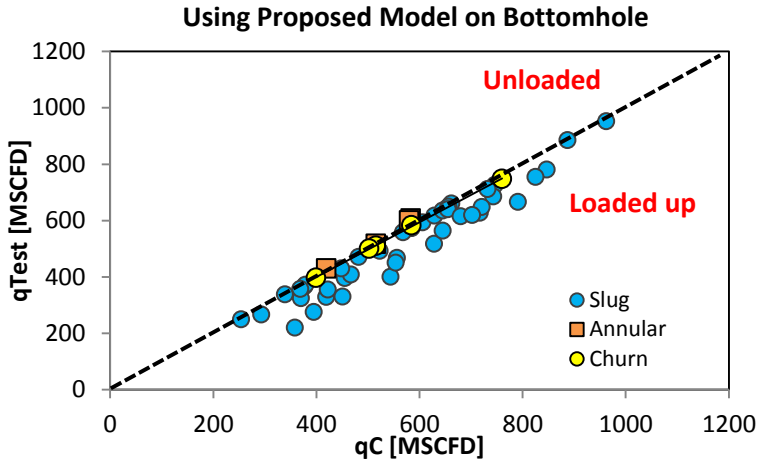

Fig. 3.17 — Relationship of actual liquid loading rate ($qTest$) with proposed critical liquid loading rate evaluated on the bottomhole (qC) suggests good correlation. Less than good estimation suggests near-loaded condition

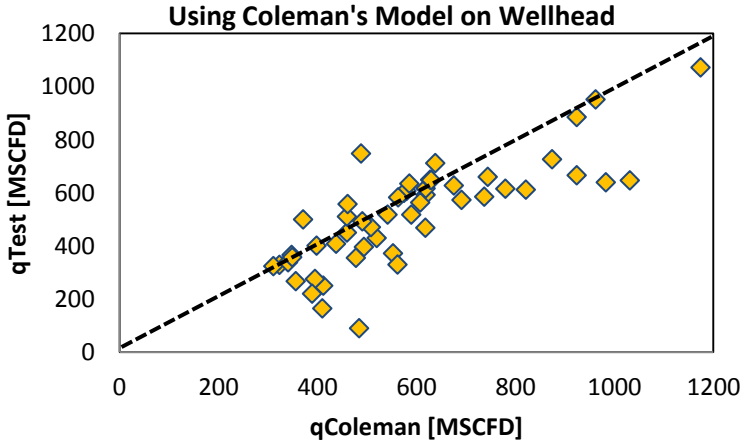

Fig. 3.18 — Relationship of actual liquid loading rate ($qTest$) with Coleman's critical liquid loading rate calculated on the wellhead ($qColeman$) shows poor correlation of Coleman's critical liquid loading rate calculated on the wellhead with actual liquid loading rate

3.4.3 Model Validation Using Veeken's Database

Veeken (2010) published data of offshore liquid loaded gas wells with substantial wellbore and reservoir information. However, several important parameters needed to calculate liquid loading rate are missing: the type of liquid flowing, liquid density, and liquid/gas ratio.

The absence of liquid/gas ratio and liquid properties data, complex trajectory of offshore multilateral wells, and different tubing diameter sizes in the wellbore, contribute to the error in liquid loading rate prediction. The deviation of the wellbore might also impact in increasing critical loading velocity calculation as suggested by Belfroid et al. (2008). Nevertheless, we can get better accuracy to predict liquid loading using Turner's original model on the bottomhole condition (Fig. 3.19) compare to Turner's modified droplet model on the wellhead condition (Fig. 3.20).

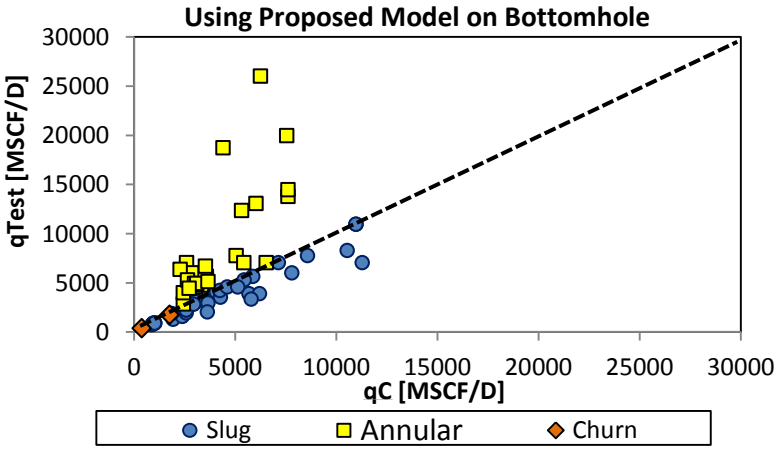

Fig. 3.19 — Relationship of actual liquid loading rate ($qTest$) with proposed critical liquid loading rate evaluated on the bottomhole (qC) indicates difficulty to match Turner's original model for wells with high inclination using the bottomhole condition

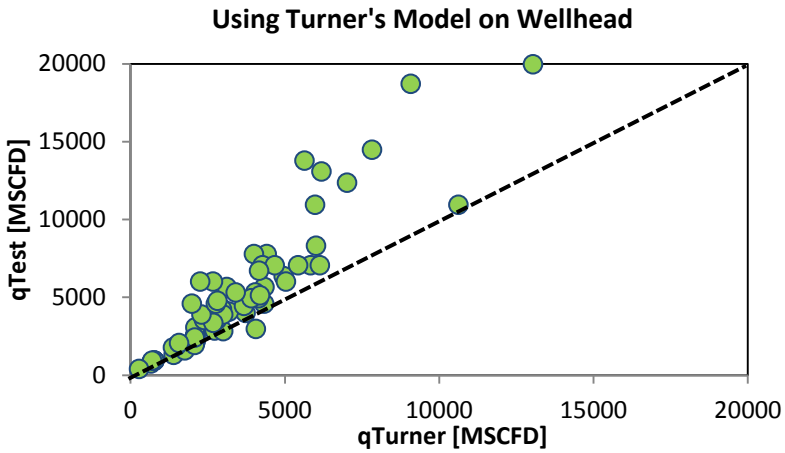

Fig. 3.20 — Relationship of actual liquid loading rate ($qTest$) with Turner's critical liquid loading rate calculated on the wellhead ($qTurner$) indicates very poor relationship of Turner's modified critical loading model calculated on the wellhead with actual liquid loading rate

CHAPTER IV

SIMULATION RESULTS AND ANALYSIS

To forecast the gas production performance of liquid loaded gas well, we integrate the reservoir inflow performance with multiphase flow in wellbore. We use condensate-gas Material Balance equation to predict the average reservoir pressure ($\bar{p}$) for the forward simulation process. We develop the analytical simulation model using Microsoft Visual Basic language.

Reservoir and wellbore models are coupled implicitly, meaning the results from the reservoir inflow equations would be used as the input for the wellbore pressure and temperature correlations using Hasan and Kabir's model. We assume that the reservoir temperature is undisturbed. Hence, the bottom-hole temperature is assumed equal to reservoir temperature at any time. The flowchart of the simulation workflow is detailed on APPENDIX D.

4.1 Data and Assumptions

We use synthetic reservoir data set, synthetic fluid properties, and wellbore data set acquired from Veeken's paper to perform the reservoir-wellbore coupled simulation. Table 4.1 through Table 4.2 explain the base case data for our simulation.

The model assumes constant Water/Gas Ratio (WGR) and constant Condensate/Gas Ratio (CGR). The control of the simulation is constant bottomhole

flowing pressure. We use the minimum wellhead pressure as the constraint (Pth_{Min}) for the simulation. Hence when wellhead pressure declines bellow $Pth_{Min,}$ we reduce the bottomhole flowing pressure by 200 psi in order to continue the production. When the wellhead pressure cannot rise above Pth_{Min} after the adjustment of the bottomhole flowing pressure, the well is considered dead and the simulation is stop.

Table 4.1 —Well #27 Dataset (Veeken et al, 2010)

Parameters	Value	Units
Well True Vertical Depth (TVD)	10990	ft
Tubing Inside Diameter	4.28	in
Bottomhole Temperature	235.4	°F
Well Deviation	0	degree
Formation Resistivity , A	103.05	Psi^2/MSCF/D
Productivity Index, J	0.097	MSCF/D/Psi^2
Wellhead Temperature	129.2	°F

Table 4.2 — Synthetic Reservoir and Fluid Properties

Parameters	Value	Units
$\bar{P}_{init}$	1600	psi
h, thickness	30	ft
$s_{w_{init}}$	10	%
ϕ, porosity	20	%
A, drainage area	300	Acre
γ_w, water gravity	1.06	-
WGR	80	STB/MMSCF
CGR	0	STB/MMSCF
γ_g, gas gravity	0.59	-

4.2 Simulation Results

Fig. 4.1 depicts the simulated gas rate (q_g) and predicted wellhead pressure (p_{th}). The volumetric Initial Gas in Place (IGIP) is 6.11 BSCF. We identified 5 different cycles of liquid loading. Each cycle ends if the wellhead pressure below the minimum tubing head pressure ($p_{th_{Min}}$=250 Psi). The well cannot maintain wellhead pressure (p_{th}) above $p_{th_{Min}}$ after 703 days, thus the well is dead, with cumulative production (G_p) 3.12 BSCF.

Fig**.** 4.2 illustrates the water rate and gas rate performance over time. Water rate profile follows the gas production rate profile as we keep Water/Gas Ratio constant and we ignore liquid accumulation effect in the wellbore model due to liquid loading.

The critical liquid loading rate calculated by the proposed method (Eq.3.1) and the critical rate calculated using Turner's method (Eq.3.3) are plotted against the corresponding wellhead pressure in Fig. 4.3. Note that, as wellhead pressure fluctuates during liquid loading, Eq.3.3 predicts erratic critical loading rate.

The simulated wellhead pressure is plotted against normalized production time on Fig.4.4. We normalize production time by using the following expression

$$t_{D_N} = \frac{t_p * q_g}{G_p} \tag{4.1}$$

The normalized production time is plotted in reverse order to illustrate the wellhead pressure drop over time. Fig. 4.4 implies that the liquid loading happens at t_{D_N} of about 0.8 for all production rates.

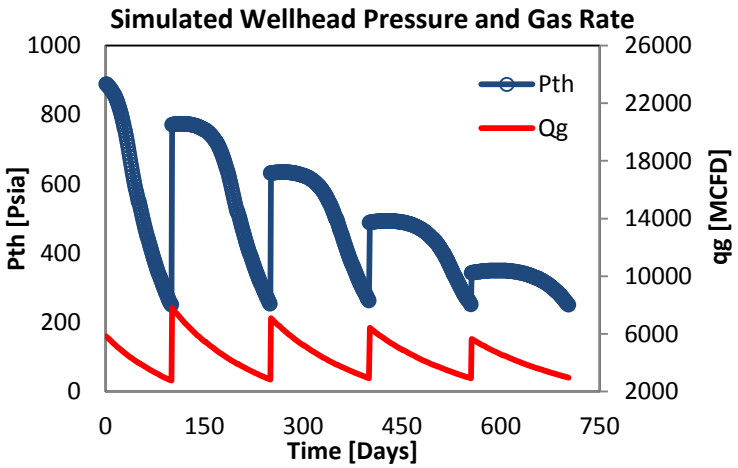

Fig. 4.1 — Simulated wellhead pressure and gas rate shows five cycles of liquid loading until the end life of the well

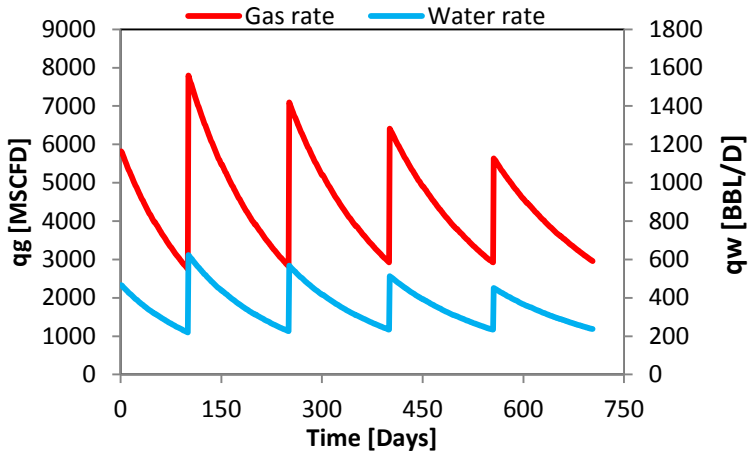

Fig. 4.2 — Simulated gas rate and water rate profile. Water rate follows gas rate profile as WGR is assumed constant and liquid accumulation is neglected in the wellbore simulation model

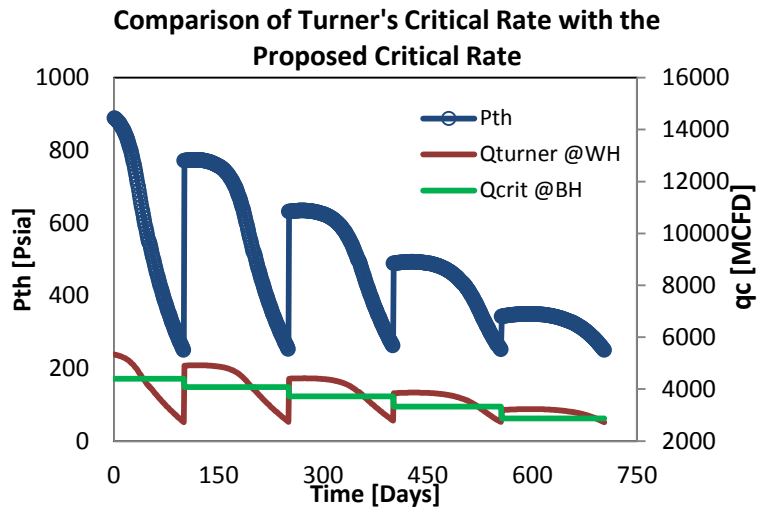

Fig. 4.3 — Simulated Turner's critical loading rate calculated on the wellhead ($qTurner$), and the proposed critical liquid loading rate calculated on the bottomhole (qC) overlapped with simulated wellhead pressure

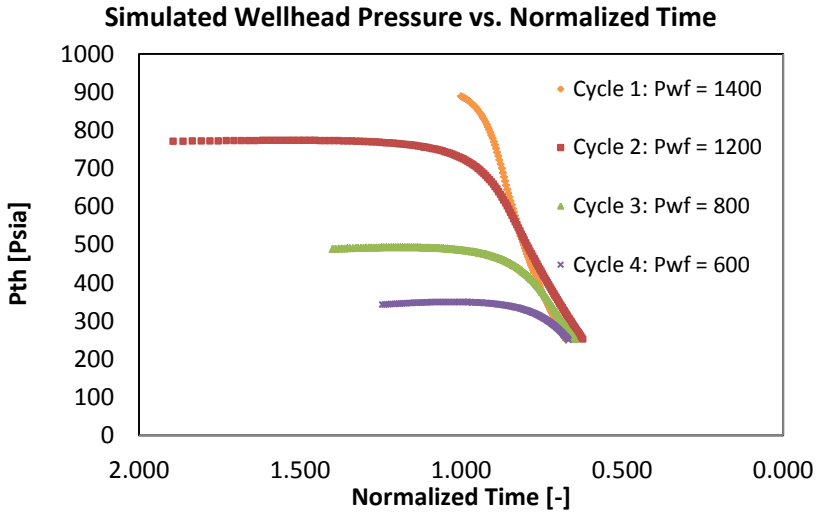

Fig. 4.4 —Simulated wellhead pressure responses of each liquid loading cycles shows wellhead pressure profile tend to merged if we plot simulated wellhead pressure against dimensionless normalized time (t_{D_N}) durring liquid loading

4.2.1 Onset of Liquid Loading Prediction

In this section, we analyze the onset of liquid loading for the first 100 days of simulation.

Turner's and Turner's family of critical velocity models theorized that Wellhead condition controls liquid loading. Therefore, using Turner's and Turner's family of critical velocity models, the onset of liquid loading (t_{onset}) happens when actual gas velocity (v_{SG}) drops bellow critical loading velocity (Fig. 4.5).

Using the Turner's model, the well is predicted to be liquid loaded after16 days, while Nosseir's model suggested the well is loaded up earlier (9 days) as inferred in Fig.4.6. Zhou's model predicts that the well is loaded up at the beginning of the production, while Coleman's method predicts that the well is unloaded. Notice that Wellhead pressure fluctuation significantly influences gas velocity and critical velocities on the Wellhead.

We observe that liquid loading initiates at the bottomhole of the wellbore where the pressure is the highest, and consequently, gas velocity is the lowest. Thus, the transition from annular flow to churn or slug flow is most likely to occur at the bottomhole first. Using this approach, our simulation suggests that liquid loading begins appearing on the 37th days (Fig. 4.7). Table 4.3 summarized the prediction of onset of liquid loading using different critical velocity models.

Fig. 4.8 depicts the profile of liquid holdup at the bottomhole and at the Wellhead. Notice that the bottomhole is flooded with liquid as liquid loading is initiated.

Fig. 4.9 illustrates the impact of sudden increase of liquid holdup to increase of pressure gradients at the bottomhole of the wellbore. However, the pressure gradient at the wellhead shows a slow decline after liquid loading is initiated (Fig. 4.10). This happens because the development of slug flow at the bottomhole leads to lower wellhead pressure, causing gas velocity at the Wellhead to increase. This leads to a gradual decrease in liquid holdup at the wellhead. In addition the liquid holdup at the bottomhole is start decreasing after liquid loading happens as illustrated in Fig. 4.7.

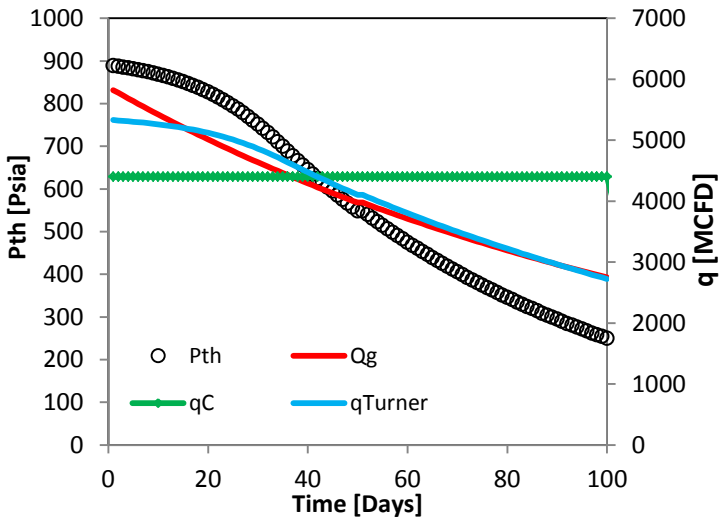

Fig. 4.5 — Simulated gas rate (Qg), Turner's critical liquid loading rate evaluated on the wellhead ($qTurner$), and the proposed critical liquid loading rate evaluated on the bottomhole (qC) of the first liquid loading cycle

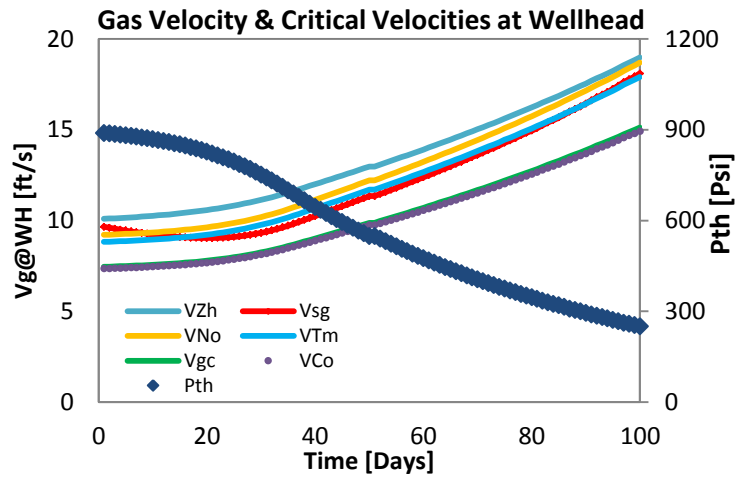

Fig. 4.6 — Simulated actual gas velocity (v_{SG}) and Turner's and Turner derivatives critical loading velocities observed on the wellhead for onset of liquid loading determination

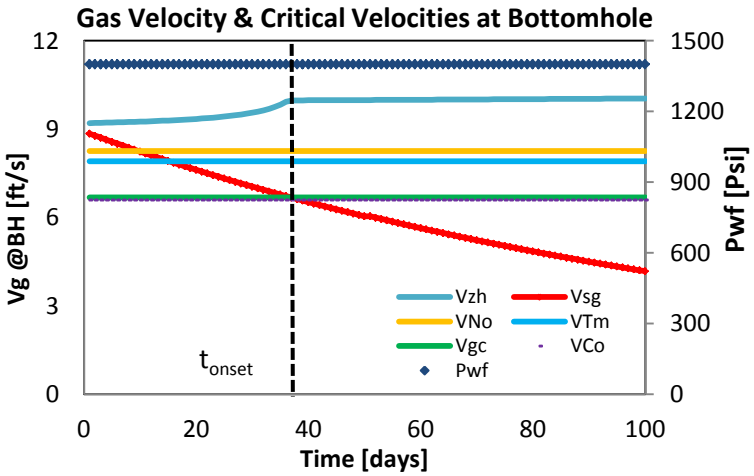

Fig. 4.7 — Simulated actual gas velocity (v_{SG}) and Turner's and Turner's derivatives critical loading velocities observed on the on the bottomhole to determine onset of liquid loading based on the proposed method

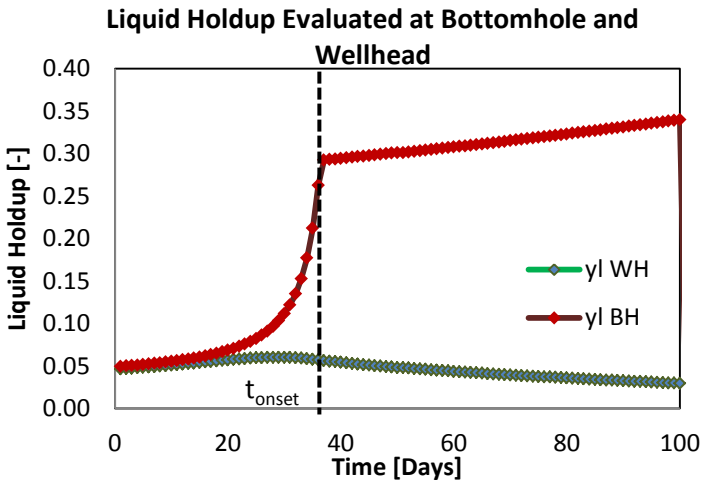

Fig. 4.8 —Abrupt increase of liquid holdup appears on the bottomhole after the onset of liquid loading

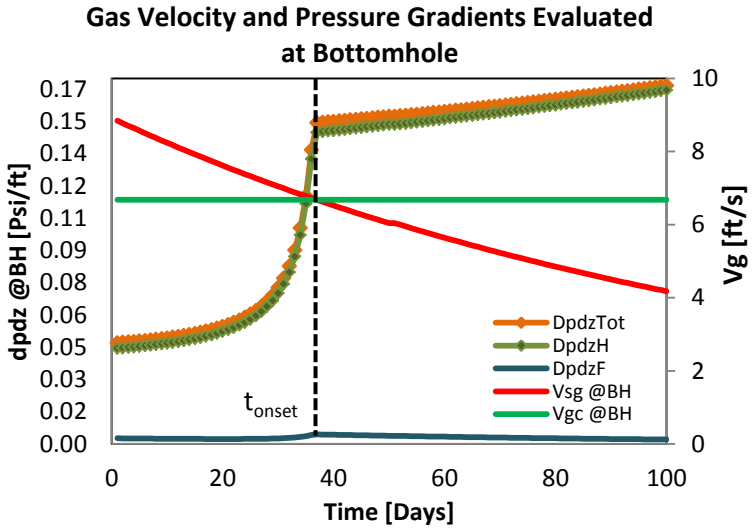

Fig. 4.9 —Pressure gradient on the bottomhole increase significantly after the onset of liquid loading

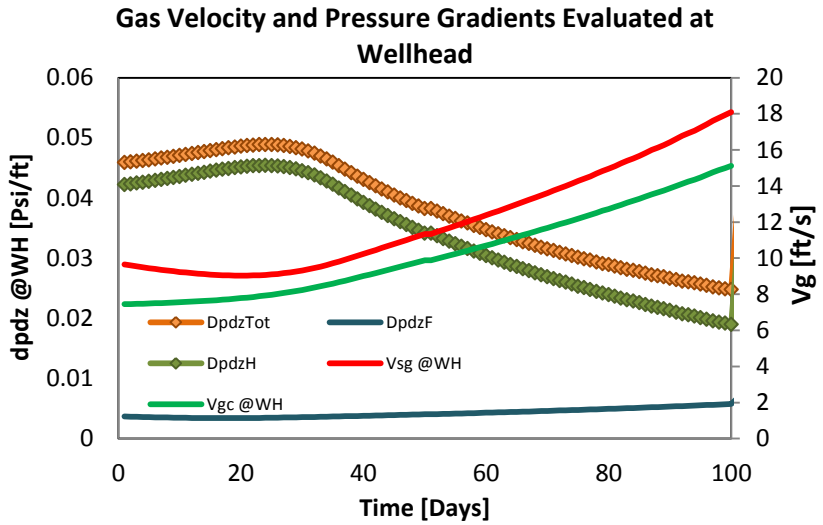

Fig. 4.10 — Simulated actual gas velocity (v_{SG}) on the wellhead increases after Slug flow (onset of liquid loading) appeared on the bottomhole of the wellbore

Table 4.3 — Onset of Liquid Loading Prediction		
Critical Velocity Model	**Onset Liquid Loading (Days)**	**Reference**
Turner	16	Wellhead
Nosseir	9	Wellhead
Zhou	0 (Initially Loaded Up)	Wellhead
Coleman	Unloaded	Wellhead
Annular-Churn Transition	37	Bottomhole

4.2.2 Design of Experiment

We conducted a 2-level multi-variables Design of Experiment (DOE) analysis to determine the variables which affect critical loading rate and onset of liquid loading; the range of variables are summarized Table 4.4. We ran the simulation by maintaining constant initial gas rate ($q_{g_{init}}$) in each case by adjusting the bottomhole flowing pressure as we varied the parameters for the DOE simulation.

Fig. 4.11 displays the Pareto chart summarizing the results of the 2-level and Plackett and Burman DOE analysis of critical liquid loading rate. The Pareto chart does not imply that variables with absolute t-test value below 95% confidence level are not influencing the critical loading rate; rather, that they are statistically insignificant within 95% of confidence.

Table. 4.4 displays the Pareto Chart of parameters which affect liquid loading rate calculation. The Pareto chart identified that tubing inside diameter (*ID*) is the most statistically dominant variable which determines the critical loading rate; productivity Index (*PI*) is identified as the second most important parameter. Wells with higher PI shows higher critical liquid loading rate (qC) since it requires higher bottomhole flowing pressure to produce the well with the same initial gas rate. The result also suggests that if liquid condensate is co-produced with water, higher Condensate Gas Ratio (CGR), would result in the smaller the critical liquid loading gas rate.

We performed similar analysis to determine parameters which affect onset of liquid loading. The positive sign associated with each of the independent variable suggests that any increase of the independent variable will resulted in increase of the dependent variables, while the opposite applies for the independent variable with negative values. Productivity Index of the well is found to be the most significant parameter for the onset of liquid loading (Fig. 4.12). Wells with smaller *PI* would experience liquid loading later than wells with higher *PI* since the critical liquid loading rate of the given wells would be lower as previously explained. Additionally, wells with

small tubing diameter (ID) would have lower critical gas rate, thus the well can produce longer before seeing liquid loading problem.

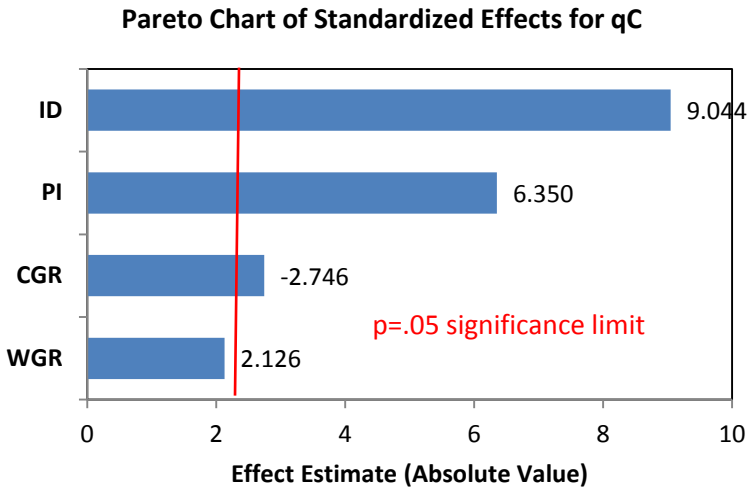

Fig. 4.11 — Pareto chart shows the effect of independent variables on critical liquid loading rate (qC) calculation

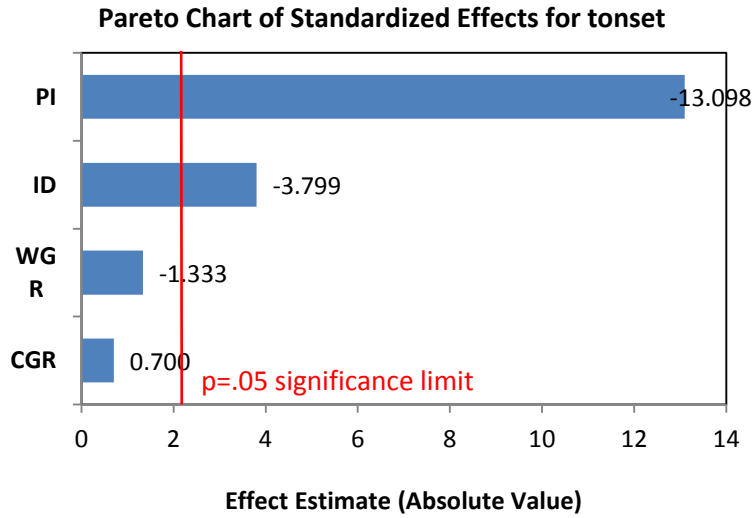

Fig. 4.12 — Pareto chart shows the effect of independent variables to onset of liquid loading (t_{onset}) prediction

Table 4.4 — Range of Variables in Critical Rate and Onset Time Prediction				
Case	PI [MSCF/D/PSI^2]	WGR [BBL/MSCF]	CGR [BBL/MMSCF]	Tubing Inside Diameter [in]
Low	0.005	10	10	4
Base	0.01	80	0	4.28
High	0.02	550	80	4.35

4.2.3 Parametric Study

To gain more understanding of the parameters which influence critical loading and onset of liquid loading, we plot the response of wellhead pressure with various parameters varied from the base case. Fig. 4.13 through Fig. 4.16 present the simulated wellhead pressure of one liquid loading cycle against independent parameters. The base case data of the parametric study is the same as the base case data summarized in Table 4.2. As suggested earlier, we found that by plotting wellhead pressure against the reverse normalized production time (t_{D_N}), the wellhead pressure response tend to merge as liquid loading start developing on the wellbore.

By increasing the productivity index, we would have higher cumulative gas production (G_p), thus the normalized production time would be smaller (Fig. 4.11). However, as suggested by the Pareto chart, wells with small productivity index (PI) would have lower critical liquid loading rate (q_C) and would have longer period of liquid-loading free production.

We varied Water/Gas Ratio (WGR) to measure the impact of WGR to liquid loading simulation (Fig. 4.12). The result advises that water would impact liquid loading

rate and onset of liquid loading calculation if Water/Gas Ratio is very high (WGR > 550 BBL/MMSCF). A different result is found with Condensate/Gas Ratio (CGR) variation as shown in Fig. 4.13. The result suggests that liquid loading rate calculation is more sensitive with variation of condensate gas ratio.

Clearly, by decreasing tubing inside diameter, critical loading rate would be lower, thus the onset of liquid loading would be find longer than the base case (Fig. 4.14). The predicted critical loading rate (qC) and liquid loading onset time (t_{onset}) are summarized on Table 4.5.

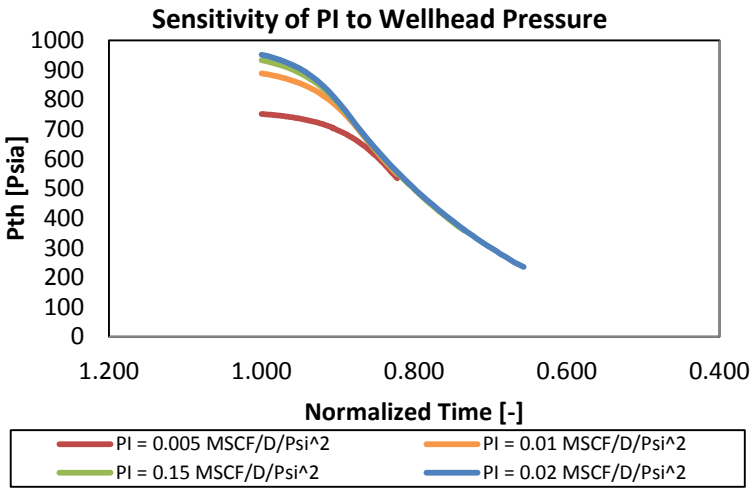

Fig. 4.13 — The effect of Productivity Index (PI) to simulated wellhead pressure response

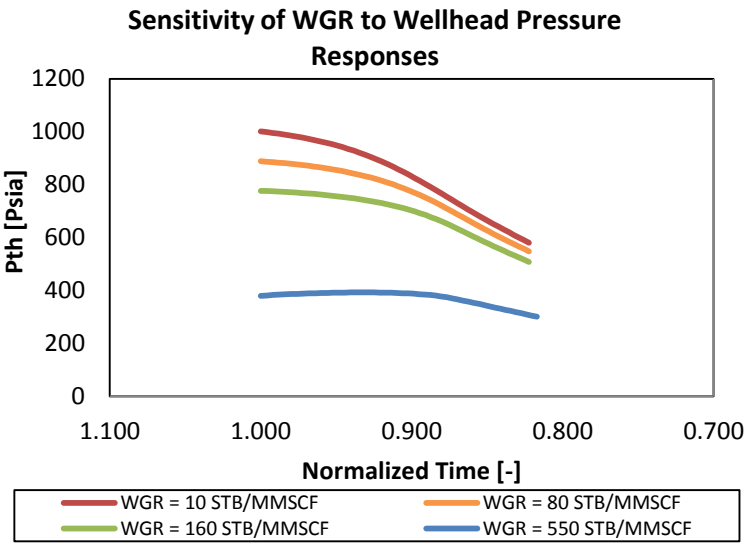

Fig. 4.14 — The effect of Water/Gas Ratio (WGR) to simulated wellhead pressure response

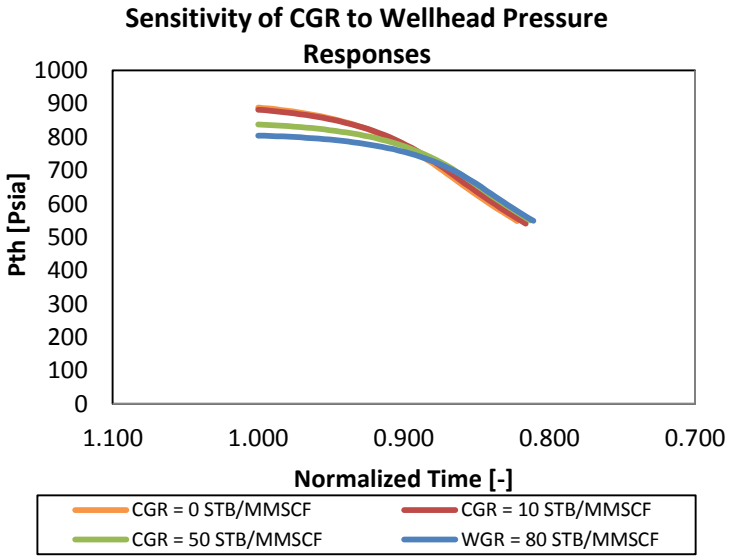

Fig. 4.15 — The effect of Cond./Gas Ratio (CGR) to simulated wellhead pressure response

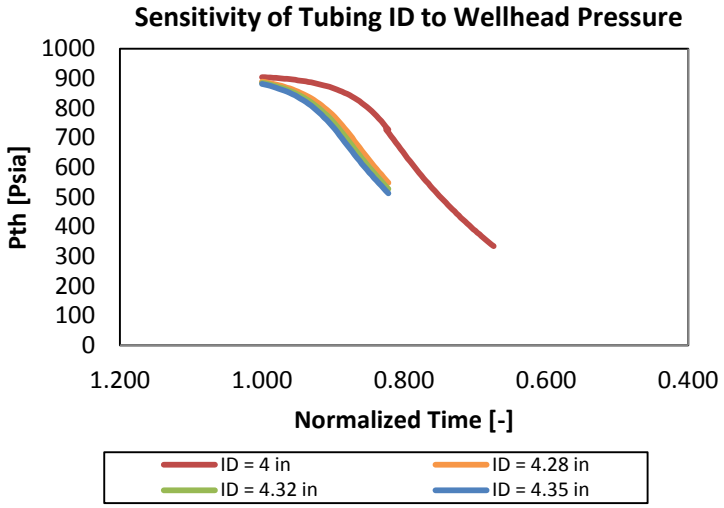

Fig. 4.16 — The effect of tubing inside diameter (ID) to simulated wellhead pressure response

Table 4.5 — Parametric Investigation Results

Parameters	Case	t_{onset} (days)	Normalized Onset Time t_{D_N} (-)	qC (MSCF/D)
Base Case	*See Table 3.1	37	8.662E-04	4410
PI	PI = 0.005 MSCF/D/PSI^2	96	8.288E-04	4045
	PI = 0.015 MSCF/D/PSI^3	22	8.775E-04	4513
	PI = 0.002 MSCF/D/PSI^4	17	8.749E-04	4561
WGR	WGR = 10 BBL/MMSCF	37	8.662E-04	4400
	WGR = 160 BBL/MMSCF	37	8.662E-04	4400
	WGR = 550 BBL/MMSCF	35	8.695E-04	4410
CGR	CGR = 10 BBL/MMSCF	37	8.662E-04	4400
	CGR = 50 BBL/MMSCF	41	8.451E-04	4253
	CGR = 80 BBL/MMSCF	42	8.396E-04	4202
Tubing ID	ID = 4 in	56	8.082E-04	3843
	ID = 4.32 in	35	8.732E-04	4483
	ID = 4.35 in	33	8.802E-04	4545

CHAPTER V

CONCLUSIONS AND RECOMMENDATIONS

5.1. Conclusions

The wellbore-reservoir connected model developed in this work was used to simulate liquid loading phenomena. Specific conclusions from our investigation include the following:

1. We addressed the critical liquid-loading determination by assuming that the unloaded well experiences annular two-phase flow throughout the wellbore. The transition from annular flow to churn or slug flow triggers the film-flow reversal; thereby, triggering liquid loading.
2. Based on full-wellbore critical loading velocity analysis, bottomhole condition is found to control the onset of liquid loading
3. The use of wellhead to predict liquid loading for highly deviated wells and wells completed with different tubing diameters is clearly misleading
4. The simulation shows steep decrease of wellhead pressure caused by slug flow development on the wellbore
5. Tubing Diameter, and Well's PI are significant parameters in qC calculation
6. Tubing Diameter, CGR, and Well's PI and are statistically important in t_{Onset} determination

7. Normalized production time can be used to recognize the pattern of liquid loaded well performance

5.2. Recommendations

1. Full scale reservoir simulation combined with the proposed wellbore models would give more accurate prediction of liquid loaded gas well performance as the flow process can be modeled more accurately.
2. Laboratory Experiment study to determine liquid accumulation process during liquid loading would is needed to further validate our approach and improve on it.
3. The reservoir inflow model and the wellbore model should be modified to model the liquid loading process of deviated or horizontal shale or tight gas well.

NOMENCLATURE

Chapter II

q_g	Gas rate, MSCF/Day
J_{PSS}	Pseudo-steady state productivity index, Mscf/Day/psi^2
$\bar{p}$	Average reservoir pressure, psi
p_{wf}	Bottomhole flowing pressure, psi
k	Reservoir permeability, md
h	Net thickness of formation, ft
T_{sc}	Standard condition temperature, 60°F
p_{sc}	Standard condition pressure, 14 psia
a	Reservoir drainage area, Acre
c_A	Reservoir shape factor, dimensionless
r_w	Wellbore radius, ft
s	Wellbore skin, dimensionless
d	Rate induced skin for gas well, dimensionless
q_{water}	Water rate, BBL/Day
q_{cond}	Condensate rate, BBL/Day
z	Gas compressibility factor, dimensionless
G_p	Cumulative dry gas production, MMscf
G_{pT}	Cumulative dry gas and liquid equivalent gas production, MMscf
γ_c	Condensate gravity, dimensionless

γ_w Water gravity, dimensionless

API_{con} Condensate API gravity, $°API$

M_{wc} Molecular weight of condensate, gr/mole

G_i Initial Gas In Place, MMscf

ϕ Formation porosity, dimensionless

S_{wi} Interstitial water Saturation, dimensionless

B_g Gas formation volume factor, RFC/SCF

p_{th} Wellhead pressure, psi

ρ Density, LBM/CUFT

u Velocity, ft/s

g_c Gravity constant, 32.17 lbm-ft/lbf-s^2

dz Length differential, ft

d Pipe diameter, in

Δp_T Total pressure gradient, psi/ft

Δp_H Hydrostatic pressure gradient, psi/ft

Δp_f Frictional pressure gradient, psi/ft

Δp_{KE} Acceleration pressure gradient, psi/ft

A_{wb} Wellbore flowing area, in^2

f_g Gas void fraction, dimensionless

y_l Liquid holdup, dimensionless

v_m Mixture velocity, ft/s

v_{SL} Superficial liquid velocity, ft/s

v_{SG} Superficial gas velocity, ft/s

f_m Mixture friction factor, dimensionless

ε Tube roughness constant, dimensionless

Λ Dimensionless Chen's parameter

Re Dimensionless Reynold's number

c_o Flow pattern constant, dimensionless

$v_{\propto}$ Rise velocity, ft/s

$v_{\propto T}$ Taylor bubble rise velocity, ft/s

$v_{\propto b}$ Bubble rise velocity, ft/s

v_{gc} Critical churn-annular velocity, ft/s

θ Pipe inclination, degree

$v_{m,db}$ Dispersed-bubbly rise velocity, ft/s

σ Surface tension, Dyne/cm

μ_w Viscosity of pure water, cp

Vv_{Tm} Turner modified critical loading velocity, ft/s

v_{Co} Coleman's or Turner's original critical loading velocity, ft/s

v_{Zh} Zhou's critical loading velocity, ft/s

v_{No} Nosseir's critical loading velocity, ft/s

R_s Solution Gas Oil Ratio, SCF/STB

B_c Condensate formation volume factor, BBL/STB

f_w Fraction of water production, dimensionless

σ_{gw} Water-gas surface tension, Dyne/cm

σ_{gc} Condensate oil-gas surface tension, Dyne/cm

σ_{od} Dead Oil surface tension, Dyne/cm

T_f Wellbore temperature, °F

T_{ei} Earth initial temperature, °F

ϕ Joule-Thompson effect lump parameter, °F/ft

L_R Distance relaxation parameter, $1/\text{ft}$

w Mass flow rate, lbm/hr

U Overall heat transfer coefficient, BTU/(hr-ft^2-°F)

k_e Conductivity of earth, BTU/(hr-ft-°F)

T_D Dimensionless temperature

t_D Dimensionless time

Chapter III

qC Critical liquid loading rate, MScf/D

$_{qColeman}$ Coleman's model critical liquid loading rate, MScf/D

$_{qTurner}$ Turner's model critical liquid loading rate, MScf/D

Chapter IV

$p_{\text{th}_{Min}}$ Minimum constraint wellhead pressure, psi

t_{D_N} Dimensionless production time

t_{Onset} Time of onset liquid loading, day(s)

Subscripts

c	Condensate
ei	Earth initial
i	Initial
$-i$	Time-step iteration
$-j$	Wellbore discretized distance iteration
l	Liquid
g	Gas
m	Mixtures
o	Oil
w	Water
$Churn$	For Churn flow
Ann	For Annular flow
bh	Bottomhole
wh	Wellhead
wf	Well flowing/Bottomhole

REFERENCES

Abdul Majeed, Ghassan H., Nimat B., Abu Al Soof et al. 2000. Estimation of gas–oil surface tension. Journal of Petroleum Science and Engineering 27 (3): pp. 197-200.

Alamu, Mhunir B. 2012. Gas-Well Liquid Loading Probed With Advanced Instrumentation. SPE Journal 17 (1): pp. 251-270.

Belfroid, Stefan, Wouter Schiferli, Garrelt Alberts et al. 2008. Prediction Onset and Dynamic Behaviour of Liquid Loading Gas Wells. Proc., SPE Annual Technical Conference and Exhibition, Denver, Colorado, USA.

Chen, Ning Hsing. 1979. An Explicit Equation for Friction Factor in Pipe. Chemistry Fundamental 18 (3): pp. 296–297.

Coleman, Steve B., Hartley B. Clay, David G. McCurdy et al. 1991a. A New Look at Predicting Gas-Well Load-Up. Journal of Petroleum Technology 43, pp. 329-333

Dousi, Niek, Cornelis A. M. Veeken, Peter K. Currie. 2006. Numerical and Analytical Modeling of the Gas-Well Liquid-Loading Process. SPE Production & Operations 21 (4): pp. 475-482.

Energy Information Agency. (2011). The Golden Age of Gas Production. Retrieved from http://www.worldenergyoutlook.org/goldenageofgas/

Fernandez, Juan J., Gioia Falcone, Catalin Teodoriu. 2010. Design of a High-Pressure Research Flow Loop for the Experimental Investigation of Liquid Loading in Gas Wells. SPE Projects, Facilities & Construction 5 (2): pp. 76-88.

Harmathy, T.Z. 1960. Velocity of Large Drops and Bubbles in Media of Infinite or Restricted Extent. Journal of Two Phase Flow and Heat Transfer. pp. 281-286.

Hasan, A.R. 1995. Void Fraction in Bubbly and Slug Flow in Downward Two-Phase Flow in Vertical and Inclined Wellbores. SPE Production & Operations 10 (3): pp. 172-176.

Hasan, A.R, and Kabir, C.S,. 2002. Fluid Flow and Heat Transfer in Wellbores. Society of Petroleum Engineers Press. Print. Houston, USA.

Hasan, A.R., Kabir, C.S,. Morteza Sayarpour. 2007. A Basic Approach to Wellbore Two-Phase Flow Modeling. Proc., SPE Annual Technical Conference and Exhibition, Anaheim, California, USA.

Hasan, A.R, Kabir, C.S., Xiaowei Wang. 2009. A Robust Steady-State Model for Flowing-Fluid Temperature in Complex Wells. SPE Production & Operations 24 (2): pp. 269-276.

Hu, Bin, Cornelis A. M. Veeken, Rahel Yusuf et al. 2010. Use of Wellbore-Reservoir Coupled Dynamic Simulation to Evaluate the Cycling Capability of Liquid-Loaded Gas Wells. Proc., SPE Annual Technical Conference and Exhibition, Florence, Italy.

Jackson, Donald F B, Claudio Juan Jose Virues, David Sask. 2011. Investigation of Liquid Loading in Tight Gas Horizontal Wells With a Transient Multiphase Flow Simulator. Proc., Canadian Unconventional Resources Conference, Alberta, Canada.

Lea, James F., Henry V. Nickens. 2004. Solving Gas-Well Liquid-Loading Problems. Journal of Petroleum Technology 56 (4): pp. 30-36.

Kang C.W., Hua J.S., Lou J., Liu W. and Jordan E., 2008. Bridging the Gap between Membrane Bio-reactor (MBR) Pilot and Plant Studies. Journal of Membrane Science 325: pp. 861–871

Masroor Ahmad, Deng J. Peng, Colin P. Halet, Simon P. Walker and Geoffrey F. Hewitt. 2010. Droplet Entrainment in Churn Flow. 7th International Conference on Multiphase Flow, Tampa, Florida, USA.

Neves, T.R., R.M. Brimhall. 1989. Elimination of Liquid Loading in Low-Productivity Gas Wells. Proc., SPE Production Operations Symposium, Oklahoma City, Oklahoma, USA.

Nosseir, M. A., Darwich, T. A., M. H. Sayyouh et al. 2000. A New Approach for Accurate Prediction of Loading in Gas Wells Under Different Flowing Conditions. SPE Production & Operations 15 (4): pp. 241-246.

Ramey Jr., H.J. 1962. Wellbore Heat Transmission. Journal of Petroleum Technology 14 (4): pp. 427-435.

Sarica, Cem., Ge, Yuan., Robert Sutton et al. 2013. An Experimental Study on Liquid Loading of Vertical and Deviated Gas Wells. Proc., 2013 SPE Production and Operations Symposium, Oklahoma City, Oklahoma, USA.

Sharma, Mukul, Agrawal, Samarth. 2013. Impact of Liquid Loading in Hydraulic Fractures on Well Productivity. Proc., 2013 SPE Hydraulic Fracturing Technology Conference, The Woodlands, Texas, USA.

Sutton, Robert P., S.A. Cox, James F. Lea et al. 2010. Guidelines for the Proper Application of Critical Velocity Calculations. SPE Production & Operations 25 (2): pp. 182-194.

Taitel, Y., Barnea, D. and A.E. Dukler. 1980. Modeling Flow Pattern Transition for Steady Upward Gas-Liquid Flow in Vertical Tubes. Journal of AIChE 33 (2): pp. 345-354.

Turner, R.G., M.G. Hubbard, A.E. Dukler. 1969. Analysis and Prediction of Minimum Flow Rate for the Continuous Removal of Liquids from Gas Wells. Journal of Petroleum Technology 246 (8): pp. 1475-1482

van't Westende, J.M.C., H.K. Kemp, R.J. Belt, L.M. Portela, R.F. Mudde, R.V.A. Oliemans. 2008. On the role of droplets in cocurrent annular and churn-annular pipe flow Journal of Heat Transfer and Multiphase Flow 33(9): pp. 595-615.

Veeken, Kees, Bin Hu, Wouter Schiferli. 2010. Gas-Well Liquid-Loading-Field-Data Analysis and Multiphase-Flow Modeling. SPE Production & Operations 25 (3): pp. 275-284.

Zeidouni, Mehdi, G.H. Movazi, Bagher Pourghasem. 2006. Performance Prediction of a Rich Gas/Condensate Reservoir Through Material Balance and PVT Behavior: A Case Study. Proc., SPE Gas Technology Symposium, Calgary, Alberta, Canada.

Zhang, He, Gioia Falcone, Catalin Teodoriu. 2010. Relative Permeability Hysteresis Effects in the Near-Wellbore Region During Liquid Loading in Gas Wells. Proc., SPE Latin American and Caribbean Petroleum Engineering Conference, Lima, Peru.

Zhang, He, Gioia Falcone, Peter P. Valko et al. 2009. Numerical Modeling of Fully-Transient Flow in the Near-Wellbore Region During Liquid Loading in Gas Wells. Proc., Latin American and Caribbean Petroleum Engineering Conference, Cartagena de Indias, Colombia.

Zhou, Desheng, Hong Yuan. 2010. A New Model for Predicting Gas-Well Liquid Loading. SPE Production & Operations 25 (2): pp. 172-181.

Zuber, N. and Findlay, J. A. 1965. Average Volumetric Concentration in Two-Phase Flow Systems. Journal Heat Transfer 87: pp. 453-468.

APPENDIX A

DETAILS OF FLUID AND HEAT FLOW MODELS

A.1 Pressure Loss Calculation

The general momentum balance equation for multi-phase compressible fluid, for the section where no shaft work is added, is expressed by

$$\Delta P = \frac{g}{g_c}\bar{\rho}_m dz + \bar{\rho}_m \frac{\Delta {v_m}^2}{2g_c} + \frac{2f_m \bar{\rho}_m {v_m}^2 dz}{g_c d} \tag{A.1}$$

Or,

$$\Delta P = \Delta P_H + \Delta P_{KE} + \Delta P_f \tag{A.2}$$

where,

$$\Delta P_H = \frac{g}{g_c}\bar{\rho}_m dz \tag{A.3}$$

$$\Delta P_f = \frac{2f_m \bar{\rho}_m {v_m}^2 dz}{g_c d} \tag{A.4}$$

$$\Delta P_{KE} = \bar{\rho}_m \frac{\Delta {v_m}^2}{2g_c} \tag{A.5}$$

In these expressions v_m and ρ_m are mixture velocity and density, g is the gravitational constant and f_m is the applicable friction factor for mixture phase

Fluid mixture density ($\bar{\rho}_m$) is calculated by adding the mass of the two phases in an unit volume. During multiphase flow, the wellbore is simultaneously occupied by flowing liquid and gas. Using f_g and f_l as the fraction of flow cross-section occupied by the gas and the liquid phase respectively, the mixture density is calculated as follows:

$$\bar{\rho}_m = f_g \rho_g + \rho_l f_l \tag{A.6}$$

and

$$f_l = 1 - f_g \tag{A.7}$$

The in-situ mixture velocity (v_m) is the total of of gas (v_{sG}) and liquid (v_{sL}) superficial velocities,

$$v_m = v_{SL} + v_{SG} \tag{A.8}$$

We used Chen (1979) correlation to calculate two phase flow friction factor (f_m)

$$f_m = \frac{1}{4log\left(\frac{\frac{\varepsilon}{d}}{3.7065} - \frac{5.0452}{Re_m} log\Lambda\right)^2} \tag{A.9}$$

In Eq. A.9 ε is the pipe roughness, d is the pipe diameter, Re_m is Reynold number for two phase flow, and Λ is a dimensionless Chen's parameter. The dimensionless parameters Λ and Reynold's number (Re_m) are given by

$$Re_m = \frac{\rho_m v_m d}{\mu_m} \tag{A.10}$$

and the dimensionless Chen parameter(Λ), is expressed by

$$\Lambda = \frac{(\varepsilon/d)^{1.1098}}{2.8257} + \left(\frac{7.149}{Re_m}\right)^{0.8981} \quad \text{(A.11)}$$

A.2 Two Phase Flow Patterns

The variety of liquid rates, gas rates, fluid properties, pipe inclination, and flow direction allows different flow patterns to exist on a wellbore. Fig 2.2 in the main thesis body illustrates the major multi-phase flow patterns in vertical upward flow – bubbly, slug, churn, and annular. Bubbly or dispersed-bubbly flow rarely occurs in gas wells.

During gas-liquid flow, gas generally moves faster than liquid because it is lighter and has a tendency to flow at the center of the pipe. Liquid phase generally flows at lower velocities than the gas phase and usually as droplets, slug, or films. As Hasan et al. (2007) explains the in-situ gas velocity can be expressed as the sum of the bubble rise velocity (v_∞) and the channel center mixture velocity ($C_o v_m$), i.e. $v_g = C_o v_m + v_\infty$. Since insitu gas velocity is superficial gas velocity divided by void fraction, i.e., $v_g = v_{sg}/f_g$, therefore, gas void fraction can be expressed by the following expression

$$f_g = \frac{v_{SG}}{C_o v_m + v_\infty} \quad \text{(A.12)}$$

The flow parameter (C_o) depends on flow regime, well deviation, and flow direction. For turbulent flow, the mixture velocity profile is relatively flat and the velocity at the center of the wellbore is 1.2 times the average mixture velocity. In bubbly and slug flow, most of the gas bubbles flow through the center of the pipe, thus C_o = 1.2 for these two flow regimes. Churn flow is characterized by high turbulence which breaks

up the Taylor bubble and cause both gas and liquid phases to be dispersed. Thus, a slightly lower value of 1.15 is used for C_o for churn flow. For annular flow Hasan et al. (2007) suggested that there is no slippage, and that C_o equals 1.0.

The flow parameters (C_o) values and bubble rise velocites (v_∞) for each flow patterns are summarized in Table A1. The rise velocity of the liquid bubble is expressed using Harmathy (1960) equation

$$v_{\propto b} = 1.53\left[\frac{g(\rho_l - \rho_g)\sigma}{{\rho_l}^2}\right]^{0.25} \tag{A.13}$$

During slug flow small gas bubbles coalesced and creating large bubbles – generally known as Taylor bubbles – that occupy almost the entire pipe cross-section. Liquid slug flowing in between the Taylor bubbles gives the name of this flow pattern. The rise velocity for a Taylor bubble is given by the following expression,

$$v_{\propto T} = 0.35\sqrt{\frac{gD(\rho_l - \rho_g)}{\rho_l}} \tag{A.14}$$

In churn flow, liquid is transported in upward waves (Masroor Ahmad, 2010). Between the waves, the direction of the film flow reverses and the film falls downward toward the next rising wave of mixtures. Churn flow is characterized by much higher mixture velocities that reduce the influence of bubble rise velocity in calculating f_g. For that reason, and for simplicity, we use Eq. A.13 to calculate bubble rise velocity in churn flow even though the shape and size of the bubbles are no longer like that of a Taylor bubble.

Annular flow exists if gas velocity in pipe is very high. Gas flows as the continuous phase while liquid flows as film on the wall or entrained as a small droplet on the gas core. The liquid moves upward due to the interfacial shear of high gas velocity and form drag on the waves and drag on the droplets. Hasan et al. (2007) suggested that there is no slippage in annular flow, thus the C_o value of annular flow is equal to 1.0.

Table A.1 — Flow Pattern Parameters for Upward Flow

Flow Pattern	Flow Parameter (C_o)	Rise Velocity (V_∞)
Bubbly/Dispersed Bubbly	1.2	$V_{\infty b}$
Slug	1.2	$\bar{V}_\infty$
Churn	1.15	$\bar{V}_\infty$
Annular	1.0	$\bar{V}_{\infty a}$

Several authors have proposed sub-classifications of vertical annular flow. Wispy annular flow happens as the gas rate is further increased, causing the entrained droplet to form coherent structures which appear like clouds or wisps in the core of the pipe. At very high gas rate, the liquid film gets thinned by the high shear force until it becomes unstable and is destroyed. In such a case, there is no liquid film, all liquid is entrained as small droplets in the continuous gas phase, analogous to the inverse of the bubble flow.

A.3 Flow Pattern Transition

Two phase flow regime and its transition criteria have been studied extensively by numerous authors. Hasan et al. (2007) examined each transition and developed criteria for each individual transition. This work adopts Hasan-Kabir approach in determining flow pattern for a particular flow condition.

Hasan (1995), and Zuber and Findlay (1965) suggested that the transition from bubbly to slug flow occurs if gas void fraction (f_g) exceed 0.25 in vertical pipe. For inclined wellbore, this transition occurs at lower void fractions. For deviated wellbores, we followed Hasan-Kabir suggestion to substitute v_{SG} by $v_{SG}/\ cos\alpha$ in Eq. A.12. Thus, the superficial gas velocity needed for transition from bubbly to slug flow is given by the following expression

$$v_{gb} = \frac{C_o v_{sL} \pm v_{\infty}}{4 - C_o} cos\alpha \tag{A.15}$$

Therefore, for co-current upward and downward flow in which C_o = 1.2 we obtain

$$v_{gb} = (0.429 v_{sL} \pm 0.36 v_{\propto}) cos\alpha \tag{A.16}$$

The positive sign applies if the direction of fluid flow is upward, while the negative sign applies for the inverse direction of flow. However, if small bubble rise velocity, v_{∞}, is higher than that of the Taylor bubble, $v_{\infty T}$, e.g. in small diameter channels,

bubbly flow cannot exist. Bubbly flow also cannot exist if mixture velocity (v_m) is higher than the dispersed-bubbly mixture velocity (v_{mdb}) given by Taitel et al. (1980)

$$2{v_{m,db}}^{1.2}\left(\frac{f}{2d}\right)^{0.4}\left(\frac{\rho_l}{\sigma}\right)^{0.6}\sqrt{\frac{0.4\sigma}{g(\rho_l-\rho_g)}}=0.725+4.15\sqrt{\frac{v_{SG}}{v_m}} \tag{A.17}$$

Dispersed bubbly flow will cease to exist if gas superficial velocity (v_{SG}) is higher than the velocity required for transition from disperse bubbly flow to churn flow to occur, or

$$v_{SG} > v_{db,c} \tag{A.18}$$

where $v_{db,c}$ is given by the following expression

$$v_{db,c} = 1.08 v_{sL} \tag{A.19}$$

Transition from slug flow to churn flow occurs if v_m exceeds v_{mdb} given by Eq. A.17 and v_{sg} exceeds the minimum superficial gas velocity suggested by Eq. A19. The transition from churn to annular flow occurs if v_{sg} is higher than the critical velocity which given by the following expression

$$v_{gc} = 3.1\left[\frac{g(\rho_l-\rho_g)\sigma}{{\rho_g}^2}\right]^{0.25} \tag{A.20}$$

Since annular flow is characterized by a gas core, a minimum gas void fraction ($f_{g_{Min}}$) of 0.6 is required to sustain annular flow.

Table A.2 summarizes the flow pattern transition conditions based on the above discussion. The two conditions shown on Table A.2 needs to be fulfilled for a particular flow pattern to exist.

Table A.2 — Unified Flow Pattern Transition Criteria

Flow Pattern	Condition 1	Condition 2
Bubbly	$v_{SG} < v_{gb}$	$v_m < v_{m,db}$
Dispersed Bubbly	$v_{SG} < v_{db,c}$	$v_m > v_{m,db}$
Slug	$v_{SG} > v_{gb}$	$v_m < v_{m,db}$
Churn	$v_{SG} > v_{db,c}$	$v_m > v_{m,db}$
Annular	$v_{SG} > v_{gc}$	$f_g > f_{g_{Min}}$

A.4 Flow Pattern Transition Smoothing

Abrupt changes of flow is physically unlikely and pattern causes discontinuity in gas void fraction calculation. Therefore, for all flow patterns except for slug and bubbly flow, we used an exponential weighted-average value for C_o derived from the fully developed C_o values of the adjoining two flow regimes. The flow parameter constant (C_o) for upward bubbly and slug flow is 1.2 (Table A.1).

For upward annular flow, the smoothed flow pattern parameter constant (C_o) is given by the following expression

$$C_{o,Ann} = EXP\left(-0.01\frac{v_{gc}}{(v_{SG}-v_{gc})}\right) + 1.2\left(1 - EXP\left[-0.01\frac{v_{gc}}{(v_{SG}-v_{gc})}\right]\right) \quad (A.21)$$

Thus, gas void fraction for annular flow is calculated as follows

$$f_{g,Ann} = \frac{v_{sg}}{C_{o,Ann}v_m + v_{\infty a}} \quad (A.22)$$

where the term $v_{\infty A}$ is given by

$$V_{\propto a} = 0.345\left[gd\sqrt{\left(\frac{\rho_l - \rho_g}{\rho_l}\right)}\right](sin\alpha)^{0.5}(1+cos\alpha)^{1.2}\left[1 - EXP\left(-0.01\frac{v_{gc}}{(v_{sg}-v_{gc})}\right)\right] \quad (A.23)$$

For co-current upward churn flow, the flow pattern parameter is smoothed by the following expression

$$C_{o,Churn} = 1.15\left[EXP\left[-0.02\frac{v_{gc}}{(v_{sg}-v_{gc})}\right] + 1.2\left(1 - EXP\left[-0.02\frac{v_{gc}}{(v_{sg}-v_{gc})}\right]\right)\right] \quad (A.24)$$

A.5 Fluid Temperature Model

An accurate estimate of fluid temperature is necessary for calculating various fluid properties and velocities. We used an analytical heat transfer model proposed by Hasan et al. (2009) to calculate fluid temperature along the well. The model is based on a general energy balance

$$\frac{dH}{dz} - \frac{g\sin\alpha}{Jg_c} + \frac{v}{Jg_c}\frac{dv}{dz} = \mp\frac{Q}{w} \quad (A.25)$$

Expressing enthalpy change in terms of temperature and pressure changes results in the following differential equation for steady-state fluid temperature,

$$\frac{\mathrm{d}T_f}{\mathrm{d}z} = C_J \frac{\mathrm{d}p}{\mathrm{d}z} + \frac{1}{c_p}\left(\mp \frac{Q}{w} + \frac{g \sin\alpha}{J g_c} - \frac{v}{J g_c}\frac{\mathrm{d}v}{\mathrm{d}z} \right) \tag{A.26}$$

Heat influx, Q, from the formation to the wellbore fluid per unit length of wellbore, is given by

$$Q \equiv -L_R w c_p \left(T_f - T_{ei}\right) \tag{A.27}$$

where,

$$L_R = \frac{2\pi}{w c_p}\left(\frac{r_{to} U_{to} k_e}{k_e + r_{to} U_{to} T_D}\right) \tag{A.28}$$

Thus,

$$\frac{dT_f}{dz} = L_R\left(T_f - T_{ei}\right) + \frac{g\ sin\ (\theta)}{C_p J g_c} - \phi \tag{A.29}$$

where, the variable ϕ lumps the kinetic energy term and the term containing the Joule-Thompson effect

$$\phi = \frac{v}{C_p J g_c}\frac{dv}{dz} - C_j \frac{dp}{dz} \tag{A.30}$$

and T_D is given, in terms of dimensionless time, $t_D = \alpha t / r_w^2$, by

$$T_D = ln\left[e^{(-0.2 t_D)} + (1.5 - 0.3719 e^{-t_D})\right]\sqrt{t_D} \tag{A.31}$$

We use a constant geothermal gradient when $T_{ei} = T_{eiwh} + g_G z$. Assuming that terms other than those containing z or T_f are constant, we obtain the following solution for fluid temperature along the wellbore,

$$T_f = T_{ei} + \frac{1 - e^{(z - z_j)L_R}}{L_R}\left(g_G sin\ (\alpha) + \phi - \frac{g\ sin(\alpha)}{C_p}\right) + e^{(z - z_j)L_R}\left(T_{f_j} - T_{ei_j}\right) \tag{A.32}$$

where z_j is the well depth where fluid temperature is known to be T_f – often this would be the bottomhole where fluid and formation temperature are usually equal.

APPENDIX B

FLUID PROPERTIES CORRELATION

The fluid properties correlations that we used to construct full wellbore critical velocity analysis is slightly modified from Sutton's (2010) and Abdul Majeed et al. (2000) works.

We calculate gas density (ρ_g) using real-gas equation

$$\rho_g = \frac{PM_g}{ZRT_{\circ R}} \tag{B.1}$$

Sutton (2010) gives the correlation to calculate condensate density using the following expression

$$\rho_c = \frac{62.366\gamma_c + 0.0136\gamma_g R_s}{B_c} \tag{B.2}$$

While water density is given by the following expression

$$\rho_w = \frac{0.999012\gamma_w + 0.000218\gamma_g R_{sw}}{B_w} \tag{B.3}$$

If the well is producing both water and liquid condensate, we calculate the liquid density using the averaging technique as follows

$$\rho_l = \rho_c(1 - f_w) + \rho_w f_w \tag{B.4}$$

Where water fraction (f_w) is determined by the following equation

$$f_w = \frac{q_w}{q_w + q_c} \tag{B.5}$$

Sutton developed water-gas surface tension (σ_{wg}) correlation as the function of fluid density and wellbore temperature as follow

$$\sigma_{gw} = \left[\frac{1.53988(\rho_w - \rho_g) + 2.08339}{\left(\frac{T_R^0}{T_c}\right)^{\left(0.821976 - 1.83785x10^{-3}T_R^0 + 1.34016x10^{-6}T_R^{0^2}\right)}} \right]^{3.6667} \tag{B.6}$$

Additionally, for gas wells which produces liquid condensate (oil) only, we use oil-gas surface tension correlation developed by Abdul Majeed et al. (2000)

$$\sigma_{go} = \left(0.056379 + 0.94362e^{-3.8491x10^{-3}R_s}\right)\sigma_{od} \tag{B.7}$$

While the dead oil surface tension, σ_{od}, is given by

$$\sigma_{od} = (1.17013 - 1.694x10^{-3}T_F^0)(38.085 - .259\gamma_{API}) \tag{B.8}$$

If the gas well produces both condensate liquid (oil) and water, we used water-gas surface tension and neglect oil-gas surface tension in the critical velocity calculation since water is heavier than oil, and water-gas surface tension is higher than oil-gas surface tension.

APPENDIX C

VALIDATION OF CRITICAL LOADING DATABASES TABLES

Table C-1 — Turner's Database Validation										
Well No.	**TVD (ft)**	**Pth (psia)**	**Pwf *(Psia)**	**Vsg @BH (ft/s)**	**Vgc @BH (ft/s)**	**Turner Status**	**BH Status**	**qTest (MSCFD)**	**qC (MSCFD)**	**qTurner (MSCFD)**
1	6404	725	1404	2.8	3.7	NLU	Slug	775	857	779
2	6739	400	1431	2.2	5.7	NLU	Slug	417	707	583
3	6529	108	212	22.5	16	NLU	Ann	568	436	306
4	6700	450	865	4.1	5.1	NLU	Slug	712	782	661
5	6770	450	865	4.1	5.1	NLU	Slug	442	464	419
6	11200	3607	5313	2.6	2.6	Loading	Slug	1525	1530	1150
7	11340	3660	5055	6.4	1.9	Unloaded	Ann	3726	1145	1142
8	11416	3340	5615	1.9	1.9	Loading	Slug	2611	4268	2412
9	11417	3540	5764	2	1.9	Loading	Slug	1814	2315	1635
10	11426	3472	5075	4.4	1.9	Unloaded	Ann	2572	1333	1108
11	11355	3338	5226	2.6	2.6	Loading	Slug	2261	2390	1623
12	11390	3455	5053	4.8	1.9	Unloaded	Ann	2769	1305	1082
13	8690	3615	4698	4.6	2	Unloaded	Ann	3890	1739	1660
14	8840	3025	3984	4.6	2.1	Unloaded	Ann	3517	1646	1604
15	11850	7405	9102	6.3	1.6	Unloaded	Ann	6946	1783	1569
16	6995	2226	2747	5.2	2.5	Unloaded	Ann	1959	975	936
17	5515	1590	2384	2.3	2.7	Loading	Slug	3009	3287	3281
18	7346	1835	2921	21.8	3.4	Unloaded	Ann	8672	1268	1239
19	8963	5056	6177	5.3	2.5	Unloaded	Ann	3376	1605	1770
20	5294	1902	2251	3.6	2.7	Unloaded	Ann	1138	878	851
21	5234	1895	2269	5.7	2.7	Unloaded	Ann	1797	876	875
22	7639	2814	3484	4.5	3.2	Unloaded	Ann	1596	1147	1216
23	7475	2783	3474	8.4	2.3	Unloaded	Ann	2939	814	834
24	7546	2574	3198	5.9	3.3	Unloaded	Ann	1943	1104	899
25	7753	2611	3347	10	2.3	Unloaded	Ann	3436	805	1082
26	8162	2556	3215	3.6	2.4	Unloaded	Ann	1550	1050	1026
27	7531	760	1641	3.8	5	Loading	Slug	1247	1396	1148
28	3278	422	851	2.7	5.3	Loading	Slug	5740	6029	5923
23a	7475	2783	3474	8.4	2.3	Unloaded	Ann	2939	814	834
23b	7475	2655	3416	11.9	2.3	Unloaded	Ann	4140	806	817
23c	7475	2406	3320	17.1	2.3	Unloaded	Ann	5820	786	770
23d	7475	2205	3256	20.5	2.3	Unloaded	Ann	6871	766	746
24b	7546	2224	2840	9.8	3.5	Unloaded	Ann	2970	1058	833
24c	7546	1839	2474	14.3	3.8	Unloaded	Ann	4485	989	755

Table C-2 — Coleman's Database Validation									
Well No.	**TVD (ft)**	**Pth (Psia)**	***Pwf (Psia)**	**Vsg @BH (ft/s)**	**Vgc @BH (ft/s)**	**BH Status**	**qTest (MSCFD)**	**qC (MSCFD)**	**qColeman (MSCFD)**
1	7812	275	548	7.5	9.4	Slug	726	746	874
2	8021	205	350	10.9	11.2	Slug	660	662	744
3	8437	212	650	5.5	8.1	Slug	685	743	737
4	8437	150	650	3.9	7.5	Slug	468	556	618
5	8042	185	355	9.3	10.3	Slug	573	585	691
6	5538	145	315	11	12.7	Slug	593	606	619
7	5538	145	315	11.4	13	Slug	617	629	619
8	6446	70	175	8.5	9.8	Slug	250	254	412
9	6026	140	223	15.9	14.4	Ann	607	583	580
10	6026	138	223	15.7	14.4	Ann	600	580	575
11	6449	130	306	11.9	13.3	Slug	635	645	586
12	6764	125	200	16.5	17.5	Churn	583	584	563
13	5678	165	329	11.2	12	Slug	649	656	628
16	6984	355	613	8.7	9.2	Slug	952	962	962
17	6034	105	182	13.9	12.9	Ann	430	419	520
18	5338	99	400	5.6	9.9	Slug	396	455	494
20	5342	43	350	5.2	10.7	Slug	329	419	323
21	5147	52	284	5.6	9.5	Slug	267	293	356
22	7763	352	663	5.5	6.3	Slug	640	655	983
23	7763	225	663	5.3	7.9	Slug	615	680	780
24	6900	94	N/A	13.9	15.8	Churn	748	760	488
25	7428	65	568	2.7	7.8	Slug	276	395	395
26	4680	59	N/A	18.5	19.1	Churn	500	502	371
27	5011	50	168	13.1	16.1	Slug	366	377	348
28	5745	39	284	6.8	12.3	Slug	324	370	311
30	6443	60	421	3	9.1	Slug	220	358	389
31	6443	90	421	4.9	9.3	Slug	355	422	478
32	6582	50	122	16.7	17.1	Slug	338	339	341
33	6898	60	N/A	3	8.3	Slug	401	544	398
34	6898	80	N/A	3.4	8.4	Slug	450	554	460
35	6351	107	257	10.9	12.6	Slug	471	482	508
36	6722	135	306	7.1	8.3	Slug	372	379	553
37	7600	131	781	3.7	7.9	Slug	518	628	590

38	6120	130	462	4	8.3	Slug	330	451	562
39	6880	82	181	16.5	19.5	Churn	511	515	460
40	6556	90	273	12.1	13.7	Slug	558	568	461
41	6301	100	362	8	11.3	Slug	493	523	491
42	4751	183	673	5.2	9.1	Slug	627	717	676
43	5065	120	202	15.4	15.1	Ann	518	515	542
44	6285	47	212	10.1	16.6	Slug	358	369	349
45	6335	315	440	11.8	12.2	Slug	885	887	924
46	8439	165	447	9.3	10.9	Slug	712	732	638
47	8158	75	450	5.3	9.7	Slug	408	467	438
48	8508	380	1100	2.9	4.9	Slug	666	791	924
49	8466	155	725	5	8.5	Slug	648	721	630
50	8466	145	725	4.4	8	Slug	564	645	608
51	8504	235	728	6	8.8	Slug	781	847	782
52	8504	225	728	5.8	8.7	Slug	755	825	764
53	8440	165	725	4.7	8.1	Slug	620	702	610
54	6796	49	244	10.5	13.8	Slug	430	448	335
55	6381	59	154	15.7	16.5	Churn	397	399	372

Table C-3 — Veeken's Database Validation									
Well No.	**TVD (FT)**	**Pth (psi)**	***Pwf (Psia)**	**Vsg @BH (ft/s)**	**Vgc @BH (ft/s)**	**BH Status**	**qTest (MSCFD)**	**qC (MSCFD)**	**qTurner (MSCFD)**
1	6562	58	1108	1.9	7	Slug	1307	1941	1405
2	6562	58	1175	1.7	6.8	Slug	1590	2401	1766
3	6562	80	712	4.3	9	Slug	742	902	662
4	6562	87	366	10.3	13	Slug	919	956	712
5	6562	87	560	6.1	10.3	Slug	919	1034	778
6	6562	87	555	6.1	10.4	Slug	919	1029	778
7	6562	80	523	6.5	10.7	Slug	848	943	700
8	6562	87	240	16.1	16.2	Churn	1766	1766	1379
9	6562	87	815	3.6	8.4	Slug	2155	2580	2112
10	6562	87	482	6.9	11.2	Slug	2402	2591	2088
11	6562	87	325	11	13.8	Slug	2508	2583	2107
12	6562	87	313	14	14.1	Slug	3073	3080	2104
13	6562	87	542	6.3	10.5	Slug	919	1025	778
14	6562	87	357	12	13.1	Churn	389	395	281
15	6562	87	1079	2.4	7.1	Slug	1943	2582	2089
16	6562	87	730	4.1	8.9	Slug	2225	2588	2099
17	6562	87	283	12.7	14.8	Slug	2508	2557	2107
18	6562	87	228	16.5	16.6	Slug	2614	2617	2107
19	6562	87	727	4.2	8.9	Slug	2225	2586	2099
20	6562	102	280	14.6	14.9	Slug	1872	1880	1497
21	10991	218	877	8.2	8.3	Slug	3532	3544	2386
22	10991	348	1223	7.4	6.9	Slug	4238	4286	2984
23	10991	218	1046	7.9	7.5	Slug	7770	7900	4414
25	10991	218	403	23.9	12.5	Ann	4591	2688	4331
26	10991	1175	2291	6.1	4.9	Slug	7063	7140	5837
27	10991	1421	4126	2.1	3.8	Slug	3885	5694	2299
29	10991	1233	2249	5.1	5.2	Slug	10948	10990	10629
32	13517	174	498	35.4	11.2	Ann	7063	5431	4677
33	13517	283	595	29.5	10.2	Ann	7063	2610	6142
35	13517	365	630	23.7	10	Ann	6004	2905	5045
36	13517	174	488	32.6	11.5	Ann	6357	2283	4966
37	9925	174	441	47.4	12	Ann	18717	4415	9086
38	9925	638	1563	9.3	6	Slug	13773	14067	5645
39	9925	653	1677	9.1	5.8	Slug	14480	16312	7826
40	9925	355	556	26.1	10.6	Ann	13067	6041	6193
42	9925	1262	2150	5.3	5	Slug	10948	10971	5982
43	9925	276	443	31.2	12.2	Ann	12361	5326	7023
44	10499	276	479	24.7	11.2	Ann	5298	2645	4044
45	10499	363	1137	8.8	7.5	Ann	4591	3040	2766
46	10499	392	527	21.1	11.4	Ann	4945	3007	3924
47	10335	435	614	19.8	10.5	Ann	6004	3516	2257
48	10417	450	579	16.8	10.6	Ann	4768	3340	2821
49	10417	336	478	21.4	11.9	Ann	4945	3116	4155
50	10417	450	1063	7.6	7.7	Slug	4062	4069	3198
51	10417	1610	4327	1.8	3.4	Slug	3885	6212	3011
52	10417	1320	3769	1.8	3.7	Slug	3355	5807	2684
24a	10417	667	2582	2.6	4.6	Slug	3532	4286	2803

24b	10827	1189	3492	2.4	3.9	Slug	8299	10551	6014
28a	10827	1233	3583	2	4	Slug	7063	11288	4281
28b	10827	725	2246	3.5	5.1	Slug	7770	8578	4005
29a	8038	667	1544	6.9	6.1	Slug	5651	5876	4346
29b	8038	493	688	14.6	9.5	Ann	5121	3666	4197
30a	12795	740	1451	6.4	6.5	Slug	4238	4252	2963
30b	13451	566	876	18.3	8.6	Ann	6710	3532	4168
30c	13451	392	637	20	10.1	Ann	5298	3028	3418
30d	13451	319	536	20.7	11.1	Ann	4591	2780	1987
31a	12795	667	887	18.9	8.5	Ann	7063	3585	5433
31b	12795	479	887	18.9	8.5	Ann	6004	3350	2680
31c	10827	319	1018	5.6	7.8	Slug	2826	2959	3006
34a	10991	522	1558	7.7	6	Slug	5651	5809	3122
34b	8448	348	1749	2.6	5.3	Slug	2967	3663	4064
34c	8337	305	494	18.2	10.8	Ann	2049	1319	1576
34d	8274	261	412	21.7	11.9	Ann	4450	2729	3677
34e	8389	290	806	8.2	8.3	Slug	2861	2870	2724
41a	8104	392	938	7.7	7.7	Slug	3991	4000	3729
41b	9980	522	798	24.5	8.6	Ann	19953	7555	13041
41c	8432	363	648	38.9	9.5	Ann	26027	6260	11516

* Calculated using Hasan-Kabir Top-Down Pressure Loss Calculation

APPENDIX D

FLOW CHART OF SIMULATION